

Developing a Thailand solar irradiance map using Himawari-8 satellite imageries and deep learning models

Suwichaya Suwanwimolkul, Natanon Tongamrak, Nuttamon Thungka
Naebboon Hoonchareon, and Jitkomut Songsiri*

Department of Electrical Engineering, Faculty of Engineering
Chulalongkorn University, Bangkok, Thailand 10330

e-mail: suwichaya.s@chula.ac.th, natanon.t@chula.ac.th, nuttamon.thungka@gmail.com
naebboon.h@chula.ac.th, and jitkomut.s@chula.ac.th

December 6, 2024

Abstract

This paper presents an online platform showing Thailand solar irradiance map every 30 minutes available at <https://www.cusolarforecast.com>. The methodology for estimating global horizontal irradiance (GHI) across Thailand relies on cloud index extracted from Himawari-8 satellite imagery, Ineichen clear-sky model with locally-tuned Linke turbidity, and machine learning models. The methods take clear-sky irradiance, cloud index, re-analyzed GHI and temperature data from the MERRA-2 database, and date-time as inputs for GHI estimation models, including LightGBM, LSTM, Informer, and Transformer. These are benchmarked with the estimate from a commercial service X by evaluation of 15-minute ground GHI data from 53 ground stations over 1.5 years during 2022-2023. The results show that the four models exhibits comparable overall MAE performance to the service X. The best model is LightGBM with an overall MAE of 78.58 W/m^2 and RMSE of 118.97 W/m^2 , while the service X achieves the lowest MAE, RMSE, and MBE in cloudy condition. Obtaining re-analyzed MERRA-2 data for the whole Thailand region is not economically feasible for deployment. When removing these features, the Informer model has a winning performance in MAE of 78.67 W/m^2 . The obtained performance aligns with existing literature by taking the climate zone and time granularity of data into consideration. As the map shows an estimate of GHI over 93,000 grids with a frequent update, the paper also describes a computational framework for displaying the entire map. It tests the runtime performance of deep learning models in the GHI estimation process.

Keywords Himawari, solar map, satellite-derived GHI, Informer, Transformer, LightGBM

1 Introduction

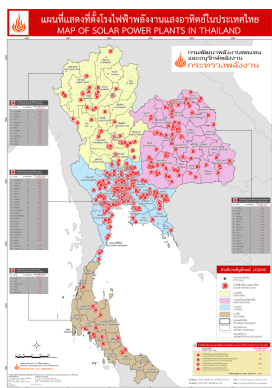
Thailand has targeted to achieve carbon neutrality by 2050 when the power grid will need to accommodate 50% share of renewable electricity generation capacity; see [Ene21]. The most recent draft of Power Development Plan 2024 (PDP2024) for 2024 – 2037 from [Ene24] proposes to add a new solar generation capacity of approximately 24,400 MWp (more than 4 times the amount issued in the previous Alternative Energy Development Plan 2015–2036 (AEDP2015) at 6,000 MWp, shown in [Dep15, p.9]. This amount does not yet include behind-the-meter, self-generation solar installed capacities of the prosumers, which is expected to increase at an accelerating rate. Solar integration into the power grid with such a sharp-rising amount will pose technical challenges to the operation and control of the transmission and distribution networks, carried out by the transmission system operator (TSO) and distribution system operator (DSO), as presented in [OB16]. Hence, TSO in Thailand will need an effective means to estimate the solar power generation across the entire transmission network, on an hourly basis, or even finer time resolution, to provide economic hour-to-hour generation dispatch for load following the total net load of the transmission, and to prepare sufficient system flexibility (*i.e.*, ramp-rate capability of the thermal and hydropower plants, or energy storage systems) to cope with the net load fluctuation due to solar generation intermittency for maintaining system frequency stability, concurrently, in its operation. For DSO, a significant amount of reverse power flow when self-generation from solar exceeds self-consumption can lead to technical concerns of voltage regulation and equipment overloading problems. The near real-time estimation of solar generation in each distribution area will enable DSO to activate proper network switching or reconfiguring to mitigate such fundamental concerns to ensure its reliable operation.

*Corresponding author

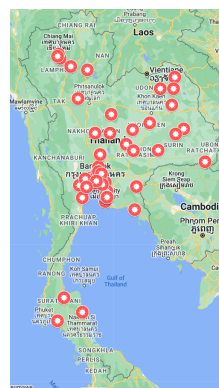
While solar energy offers a clean and virtually infinite alternative to fossil fuels, its dependence on sunshine makes it susceptible to fluctuations in weather patterns. This variability, potentially exacerbated by climate change, necessitates the development of accurate solar forecasting technology. The reliability of these forecasts directly impacts the planning (pipeline) of solar photovoltaic (PV) systems, ensuring they are integrated efficiently into the power grid, and also influences the operational settings required for various energy applications.

Global horizontal irradiance (GHI) estimation services provide crucial information in the solar energy industry. These services often provide estimated GHI for a desired location by using a combination of weather models, satellite imagery, and measurements from ground stations. These GHI databases can be divided into i) satellite-derived databases where GHI data were estimated from satellite imagery products, ii) ground-based measurements containing GHI recorded from available monitoring stations, and iii) reanalysis datasets that fuse weather estimates from atmospheric models with historical observations, including GHI data. According to [PWRA⁺16], Table 6 in the Appendix lists some satellite-derived solar irradiance services that differ from the methods they use and service coverage, dependent on the satellite. Some of the leading services that provide estimates of solar irradiance and power forecasts with global coverage can be described as follows.

SolarAnywhere provides a core technique called the SUNY model developed in the works from [PH13, PIM⁺02, PSH⁺15, PSK⁺18] that uses satellite imagery and numerical weather predictions to better calculate irradiance under cloudy conditions. SolarGIS by [SC10] uses a semi-empirical solar radiation model with data from satellites for explaining cloud properties. The service also provides site adaptation of SolarGIS data to improve the quality using ground measurements. PVWatts by NREL; see [Dob13], has an interactive page where the user can input a desired location and PV panel's parameters to calculate monthly solar irradiance and PV power. [So24] offers solar radiation maps in 15-min resolution. The method relies on HelioClim-3 persistence forecast of a clear-sky index and the use of the Meteosat satellite. SolCast service, detailed in <https://www.solcast.com/irradiance-data-methodology>, provides solar irradiance forecasts and historical data in several time resolutions. It uses NOAA, EUMETSAT which covers the continental US, Europe, and Himawari-8 satellite from JMA, which covers Asia and the Pacific, to gather information about cloud opacity and weather conditions. The methodology of producing GHI estimates consists of the SolCast cloud model and the REST2v5 clear-sky model. The SolCast cloud model takes historical and forecast data of geostationary meteorological satellite (GMS) and NWP inputs for 14 days ahead. The cloud opacity extracted from satellite cloud detection algorithms is combined with NWP inputs to account for mixing effects from weather artifacts. The validation of Solcast was presented in <https://www.solcast.com/validation-and-accuracy> for all climate conditions where sites are grouped by continent. The overall normalized MAE and RMSE of SolCast 2023 based on all 207 sites were 10.33% and 15.99%, respectively. The service also provides the SolCast Rooftop PV model, which estimates PV power when users provide PV metadata such as location, capacity, and panel tilt angle.



(a) The total on-grid solar plant capacity is 2,640 MW.



(b) 53 solar plants with ground measurements.

Figure 1: Solar power plant data in Thailand (as of March 2024). Photo credit: Renewable energy and conservation GIS of Thailand <https://gis.dede.go.th/>.

While these aforementioned companies provide a wide range of services and use advanced algorithms with several sources of input data, it boils down to the cost of acquiring these solar data for a regional application as the cost often varies with the number of sites. As of March 2024, Thailand has 552 on-grid solar power plants with a total capacity of 2,640 MW, shown in Figure 1 (a). Among these solar sites, Figure 1 (b) shows 53 solar sites fully equipped with ground measurements that participate in our study. To accommodate solar energy applications in Thailand in an operational setting, we aim to develop our solar map that frequently estimates satellite-derived GHI across the country using satellite imagery and local ground measurements. The cost of acquiring irradiance estimates across Thailand (93,061 grids) through commercial services in an operational setting (every 30 minutes) is high as compared to the cost of developing our own platform. For this reason, we study the literature on satellite-derived GHI estimation techniques in the following sections.

1.1 Physic-based and empirical methods

Traditionally, physical models use satellite information to solve the radiative transfer model, which simulates how radiation moves through absorption and scatter processes in the Earth's atmosphere. Empirical techniques rely on the statistical relationship between atmospheric parameters and ground observations. The two approaches have been merged into semi-empirical models, which analytically describe a relationship between solar radiation and aerosols in the atmosphere while using satellite information to empirically retrieve the cloud index.

Methods in this group quantify how much clouds and other particles in the atmosphere affect the incoming solar radiation by compensating with a clear-sky scenario. This relationship is often parametrized in physical parameters such as aerosol optical depth (AOD), reflectance, surface albedo, which can be derived from satellite imagery. The Heliosat model is a semi-empirical method with a core principle that combines a clear-sky model with a cloud index through a piecewise-polynomial relationship. [Dag05] used Heliosat algorithm and calculated a new cloud index from reflectivity derived from the Meteosat satellite where a modification was made on computing the ground reflectivity to save computing time. [KBSH18] extracted the brightness temperature difference from various bands of INSAT-3-D satellite to calculate the all-day index as information of cloud, dust, and fog. The GHI estimation relied on the Heliosat-2 model and was validated on ground measurements in India. The RMSE ranged from 48 to 128 W/m^2 under sky conditions with dust and fog. [VPN⁺23] presented an improvement over the MAGIC-Heliosat method on calculating apparent reflectance to compute the cloud index. The results were validated with ground stations from the baseline surface radiation network (BSRN) in Australia and Japan. The method's performance varied according to evaluation on hourly, daily, and monthly averaged data with RMSE of 161, 80, and 70 W/m^2 , respectively.

While the Heliosat model is a well-known method, there are several other semi-empirical approaches for GHI estimation. [QWL⁺18] showed that Yang's hybrid model (YHM) performed best with RMSE of 27.94 W/m^2 when compared to ANN on datasets in China. The physical method YHM relies on the radiation-damping processes, *e.g.*, Rayleigh scattering, aerosol extinction, absorption by ozone, water vapour and permanent gas. These atmospheric variables were derived from MODIS satellite. [QHM⁺19] presented a mathematical formula of GHI as a function of irradiance with zero surface albedo, global reflectance function of atmosphere and surface albedo, which can be derived from Himawari-8 satellite. The results were validated on 3-year ground station data in Australia with MAE of 55.8 W/m^2 and RMSE of 91.7 W/m^2 . The GHI model with explicit surface albedo was later used in [QHM⁺21] but all irradiance components were calculated by pre-computing Look Up Table and using radiative transfer model (RTM). The GHI estimation results were validated on data in Australia with an MAE of 54.7 W/m^2 and an RMSE of 90.3 W/m^2 . [BS21] computed the cloud indices using the surface albedo extracted from eight-band imagery of Himawari-8. These cloud indices were converted to clear-sky indices (for all eight bands), and the eight-band clear-sky indices were optimally weighted. The results were validated using data in Singapore, where the scatter plot between the ground-observed clear-sky index and the satellite-estimated values was improved.

The accuracy of semi-empirical methods varies during cloudy periods when models might not differentiate clouds' impact on irradiance. However, the methods typically require less computational demand than physical models, so they can be applied to a wide region where calibration might be needed.

1.2 Site-adaptation techniques

The site-adaptation technique adjusts satellite-derived GHI by incorporating available ground measurements to provide estimates at a target location. The correction techniques involve linear multiple regression, distribution mapping (quantile or kernel density distribution), adjusting atmospheric parameters used in the satellite retrieval process, and machine learning techniques; more details in [PWRA⁺16, PFPS⁺20].

[HV22] acquired Himawari-8 satellite images from JAXA and historical data of MERRA-2 product as inputs for REST-2 clear-sky model. The GHI estimation improvement relied on adjusting polynomial coefficients in the Heliosat algorithm, cloud albedo selection and linear bias removal as the site adaptation technique. The results were tested with hourly-averaged ground GHI in Taiwan with MAE of 38.74 W/m^2 and RMSE of 57.42 W/m^2 .

Site adaptation techniques using nonlinear models from machine learning approaches can be found in [STAK22]. The estimated GHI from the Copernicus atmospheric monitoring service (CAM-Rad) service and then corrected the value by calculating a perturbation from ML methods using solar zenith angle, AOD, water vapor, ozone, and cloud information as inputs. Overall, the two best performances were obtained by tree-based models (XG boost and random forest), which yielded an RMSE of 56-57 W/m^2 . [VSDL⁺23] used estimated GHI from HelioClim3, clear-sky index, and zenith angle as inputs for gradient boosting model to correct in both spatial and temporal domain.

Neural network techniques, presented in the next section, can capture a complex relationship between the satellite data and the corresponding ground-based GHI measurements.

1.3 Neural network techniques

Deep learning (DL) has become a leading trend in solar energy estimation due to its data-driven nature. It enables the parameters in an artificial neural network (ANN) to be fine-tuned according to the collected data; resulting in less manual customization of input features compared to the previous approaches that rely on the physical and meteorological information.

Satellite data is the key to extending the coverage of solar forecasting to entire countries. However, the database stations used as the reference for implementing and evaluating solar forecasting are often relatively sparse (e.g., [AMOG14] use only five stations), and the operation and installation can be costly. [SL18] address this limitation by using satellite-based GHI measurements in training, which offer the global irradiance information in Europe and USA; and this work shows that LSTM has the best performance among ANNs but is at a similar level to gradient boosting regression (GBR). Similarly, [YCZ19] tested LSTM on the NSRDB database (USA). Nevertheless, [QWL⁺18] found that an ANN can still be outperformed by a physics-based model with high-quality inputs, e.g., Yang hybrid model with meteorological and MODIS satellite data, while cloud fraction and solar zenith angle were found the parameters that highly includes the model accuracy.

Subsequent works further utilize the spatial information from satellite data as the reference to improve the model learning, e.g., solar radiation images in [YDA⁺20] and satellite-derived GHI in [NIK21]. The ground measurements are discontinuous and sparse, which can be inadequate to represent the regional characteristic of the estimated GHI; see [JLQ⁺19]. Utilizing the spatial information, e.g., cloud mask [NIK21], spectral images [JLQ⁺19, YDA⁺20], infrared images [AMR21], and satellite images [GCM⁺22], as inputs can promote the continuity. To process the spatial information, these works [JLQ⁺19, YDA⁺20, AMR21] attach convolution neural networks (CNN) for image feature encoding. Advanced CNN architectures are used as the IrradianceNet [NIK21] and as the STUNet [GCM⁺22] that employed ConvLSTMs and 3D-CNNs as image encoders, respectively. The time-series dynamics between satellite images are used in addition to the spatial information as an additional set of inputs. In such cases, LSTM-based models are often used to derive the forecast irradiance in the future timestamp [AMR21, NIK21]. Fusing sky and satellite images can improve forecasting accuracy [PAL23], which outperforms other methods that use only sky or satellite images. However, the sky-image based methods [FZ20, PAL21, PHAL22, LZC⁺23, ZWSW23, PAL23] focus on single-site forecasting only, which is not suitable for providing the GHI estimates at national level.

Although these satellite-based methods [QWL⁺18, SL18, JLQ⁺19, YDA⁺20, AMR21, NIK21, GCM⁺22] are promising, they are not applicable in our settings. Specifically, our system promises near real-time solar forecasting for 93,061 grids across Thailand, in which the system first acquires the satellite images from Himawari-8 provided at 10 minutes resolution, and then the satellite-derived GHI estimates are calculated and used to generate the solar map for every 30 minutes. As such, the target data-driven model has to offer a good trade-off between accuracy and efficiency. Thus, our work departs from the previous methods in the following aspects:

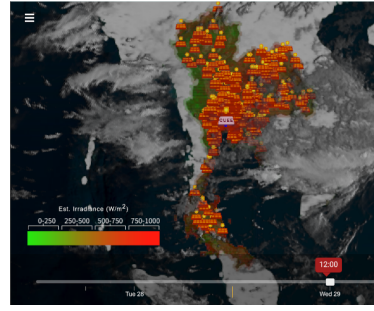
- *Input data and parameters.* Unlike previous studies [QWL⁺18, JLQ⁺19] that rely on a number of terrain and atmospheric parameters, our model relies primarily on cloud data, with time-based features and the altitude parameter.
- *Learning reference.* Satellite-derived GHI from a physical-based method is used as the reference in model learning such as [SL18, YDA⁺20, NIK21], but these references are rather indirect compared to the ground GHI measurements. Our setting tunes the model towards the GHI ground measurements.
- *Runtime requirement.* Unlike the CNN-based methods [JLQ⁺19, YDA⁺20, AMR21, NIK21, GCM⁺22] whose CNN operation performs window sliding in each grid, we try to avoid such operation, not only because of the runtime requirement, but also to retain the details of each grid area that is roughly the size of a sub-district in Thailand ($\approx 4\text{km}^2$).

Our key contributions are as follows.

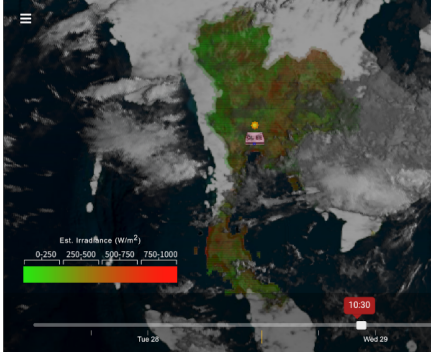
1. A clear-sky model for Thailand's weather condition. We improve the Ineichen & Perez clear-sky mode by re-estimating the Linke Turbidity using nonlinear regression. This is achieved by fitting clear-sky irradiance curve where T_L is parameter using the collected ground measurements of GHI from 53-station data.
2. A methodology that exploits deep-learning or tree-based models to capture a complex relationship between satellite cloud and GHI. To find the best model, we benchmark LSTM, Informer, Transformer, and LightGBM (LGBM) for GHI estimation. Additionally, we improved Informer and Transformer particularly for this application. For LSTM and LGBM, we study the impact of input features. Our findings indicate that all these models exhibit overall performance comparable to commercial service X, a widely recognized industry benchmark. Our implementation are provided at <https://github.com/energyCUEE/solarmap-DL-2024>.
3. A framework that operates in almost real-time implementation (30 minutes) and displays the estimated results across Thailand. Additionally, we provide the real-time solar energy map from the estimated irradiance map at hourly, monthly, and yearly resolution. This solar map can be useful for planning and operating solar energy production.



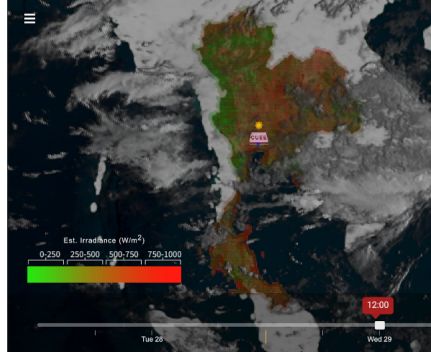
(a) Grid information



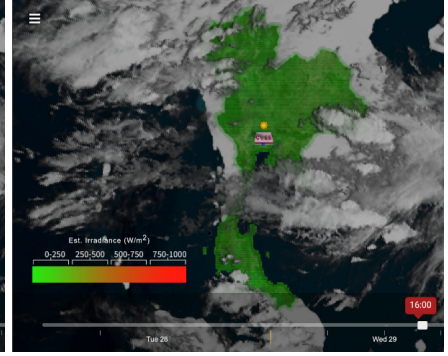
(b) Registered solar sites



(c) at 10:30



(d) at 12:30



(e) at 16:00

Figure 2: Thailand solar map displayed on www.cusolarforecast.com: (a) Estimated irradiance and generated power on a selected grid are shown. (b) There are 576 registered solar sites with known installed capacity, as shown in the orange icons. (c)-(e) Solar map displays the estimated ground irradiance at various times.

2 Thailand solar map

Our Thailand solar map platform is currently running at <https://cusolarforecast.com/>, where the methodology is a machine learning model that takes input of cloud index, geographical location, and clear-sky irradiance to produce the GHI estimate. The random forest model was implemented from 2022 to June 2024. Our continuing plan of updating the model has been discussed in [SWH⁺24], and the goal of this paper is to improve the model, considering other tree-based and deep-learning models. The service is currently running under the deep learning model, the Informer, as to be presented subsequently in Section 4.3. This section describes the map requirement and the available input data resources for developing the GHI estimation model.

2.1 Specification

Thailand solar map is required to provide the following features to support the service displayed in Figure 2.

1. The map displays at $2.4 \times 2.4 \text{ km}^2$ resolution within Thailand boundary, and contains 93,061 grids. The map intensity shows the estimated GHI that accounted for cloud information across Thailand and updates every 30 minutes.
2. The PV icons mark the locations of installed solar power plants, while the CUEE icon is our solar rooftop 8 kW at our research institution (Faculty of Engineering, Chulalongkorn University). The system shows estimated solar power and the cloud index amount extracted from Himawari-8 satellite images at the grids with solar sites installed.

In this solar map, we use the information on solar power installed capacities and locations, published on the website of the Office of Energy Regulatory Commission (ERC) at <https://www.erc.or.th/en>, together with the estimated GHI from our models being updated every 30 minutes by using the cloud images received from Himawari-8 satellite, to estimate solar generated power across Thailand. The current updating frequency of 30-minute intervals is chosen to be consistent with the time resolution of the Unit Commitment program run by TSO. The solar map will also be designed to give convenience to aggregate estimated solar energy within a specified region, for example, in each control region, sub-region of TSO, or substation service area of DSO, employing spatial ensemble techniques thereafter.

2.2 Data resources

Ground GHI solar sites There are 576 solar sites registered to the Energy Regulatory Commission of Thailand (ERC), where information on locations and installed capacity are provided. Ground measurements of GHI and satellite cloud data

are required for model training and validation among these sites. Figure 1 (b), shows 53 solar farms that record 15-minute average of solar irradiance, solar power, ambient and PV module temperature measurements from October 2020 to June 2023. The pyranometer model of solar irradiance measurement is SMP 6 (ISO 9060 spectrally flat class B). To ensure data quality, a pre-processing pipeline was implemented.

Initially, data was filtered to retain only daytime measurements. GHI values were restricted to a physically realistic range of 0 to 1400 W/m². Dates with excessively low average daytime GHI were discarded. This step aimed to eliminate periods with insufficient solar radiation or inaccurate measured values. Dates with missing data periods exceeding six hours were entirely removed. Shorter data gaps were filled using linear interpolation. Last, a manual inspection of GHI data and associated variables for consistency was performed. As a result of this quality control process, three of the original 56 sites were unsuitable and excluded from the analysis. The remaining 53 sites were deemed sufficiently reliable for this study.

Himawari-8 The 8th Himawari geostationary weather satellite operated by the Japan Meteorological Agency (JMA) provides 16-channel multispectral images that capture visible light and infrared images of the Asia-Pacific region. A C-band satellite dish and receiving station have been installed at our research institution, CUEE, since February 2022; see Figure 3. There are three types of cloud products: composite images, cloud masks, and colored images available at <https://himawari.optemis.space/archives>. We employ cloud mask images and the R-channel of the composite image that has been processed for sun zenith correction and enhanced for smoothness. The R, G, and B channels correspond to 0.6, 0.8, and 10.8 μm wavelength, respectively. Both the cloud mask and R-channel images have 1670 × 1725 pixels with the resolution of 2 × 2 km² covering Thailand area (approx. 20.6-5.4°N, 97.1-106°E), and are released every 10 minutes. These images in TIFF format contain geographical information. Given an inquired latitude and longitude, we can extract the cloud intensity at the corresponding pixel and convert it to cloud index as CI_M (from cloud mask) and CI_R (from R-channel) as follows.

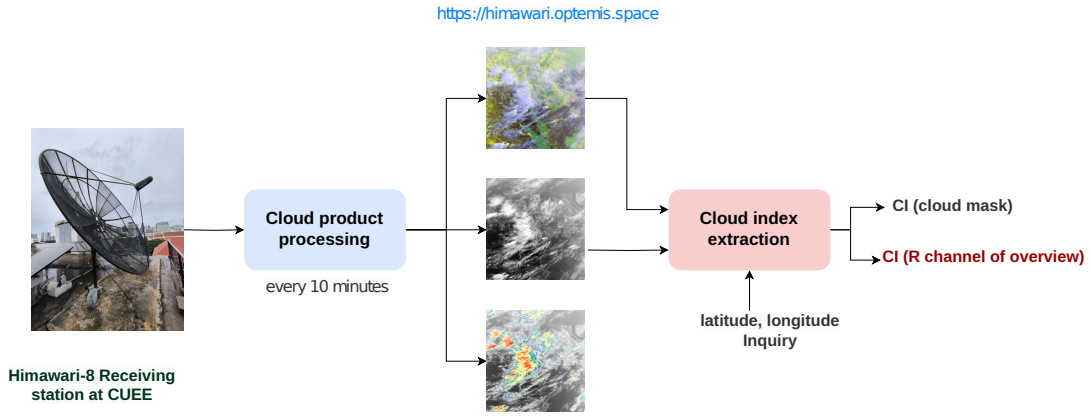


Figure 3: Himawari-8 receiving station at CUEE and cloud index processing system.

The data during the period of satellite outage or error image scan are flagged to be imputed. If the imputation period is small, a simple interpolation from nearby data points is performed, while the missing data in a long period are removed from the study.

Cloud index extraction In [PPGB13], the cloud index is calculated by

$$CI = \frac{X - LB}{UB - LB}, \quad (1)$$

where X is the pixel intensity of interest (0-255); UB and LB are the upper and lower bound of the dynamic range at a given point in time and space. In our experiment, LB is zero, and UB is 255. The cloud indices computed from cloud mask, CI_M , and R channel, CI_R , were plotted versus the clear-sky index $k(t) = I(t)/I_{ch}(t)$ shown in Figure 4, suggesting that CI_R has a stronger anti-correlation with $k(t)$ than CI_M .

Pre-processing steps were applied to cloud images and extracted cloud index (CI) data to ensure alignment with the target variable, GHI measurements. Initially, satellite images containing significant areas of bad scan (black area) were discarded. For each day, the first and last cloud image within the 7:00 to 17:00 timeframe were identified. Missing cloud images within this range were imputed using a forward-fill method. To accommodate the GHI estimation model's requirement for five lagged CI values, a backward-fill approach was employed for the first five time steps. For the imputed date-time between 5:00 and 6:00, zero-filling was applied; otherwise, backward-filling from the first image's CI value was utilized.

To train and infer a GHI estimation model, we must extract CI at a pixel of cloud images that best represents the desired location using GeoTIFF data to find the nearest pixel whose coordinate (latitude /longitude) is closest to the coordinate of interest.

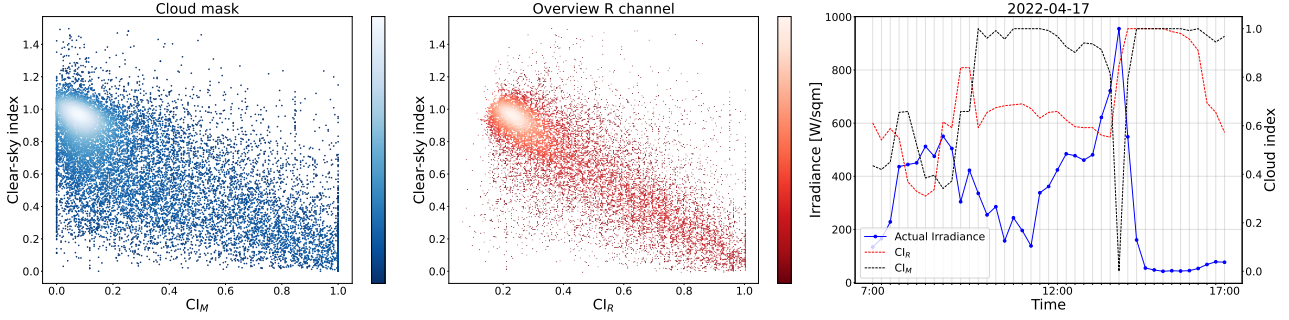


Figure 4: Cloud index computed by eq. (1). The GHI time series drops to small values when the cloud index is high.

Re-analysis weather data from NWP (numerical weather prediction) model We currently subscribe to the *Meteo Monitoring* and the *Meteo historical* services from <https://www.soda-pro.com/>. The Meteo monitoring service provides day-ahead GFS weather forecasts by the National Centers of Environmental Prediction (NCEP). At the same time, the Meteo historical contains reanalysis data of solar irradiance and temperature estimates (denoted as I_{nwp} and T_{nwp}) with a resolution of 15 minutes retrieved from the MERRA-2 model (Modern-Era Retrospective analysis for Research and Applications). For training, we incorporate the MERRA-2 GHI and temperature as part of the features for GHI estimation models at 53 solar locations.

Cloud data, NWP data, and GHI measurements overlapped from April 2022 to June 2023, resulting in our dataset of 22,906 days or 1,195,257 samples.

3 Methodology

3.1 Ineichen clear-sky model

A clear-sky model provides a GHI value at a given time and location under a clear-sky assumption. It typically takes date-time to estimate the solar zenith angle or the sun position and uses the location's coordinate to acquire the altitude and other atmospheric parameters. Benchmarking of 75 clear-sky models can be found from [GBL⁺19, YB20, SBG⁺21, BBZ⁺20], where it was reported that the REST2 model is among the best-performing models in the equatorial zone. At the same time, it requires several atmospheric parameters such as aerosol optical depth, total ozone, nitrogen dioxide amounts, or aerosol single-scattering coefficient. Among these 75 models, simplified-Solis model [Ine08a], Kasten, and Ineichen & Perez models require fewer numbers of physical input parameters.

In this paper, we consider the Ineichen & Perez clear-sky model [IP02] due to its simplicity in acquiring only one atmospheric parameter, the Linke turbidity. The model is described by

$$I_{\text{clr}}(t) = a_1 I_0 \cos \theta(t) e^{-a_2 \text{AM}(t)(f_{h_1} + f_{h_2}(T_L - 1))}. \quad (2)$$

The extraterrestrial irradiance constant, $I_0 = 1366.1 \text{ W/m}^2$ is the theoretical value of irradiance on the Earth's surface if the Earth were not surrounded by an atmosphere. The altitude of a desired location, h , is used for computing the constants:

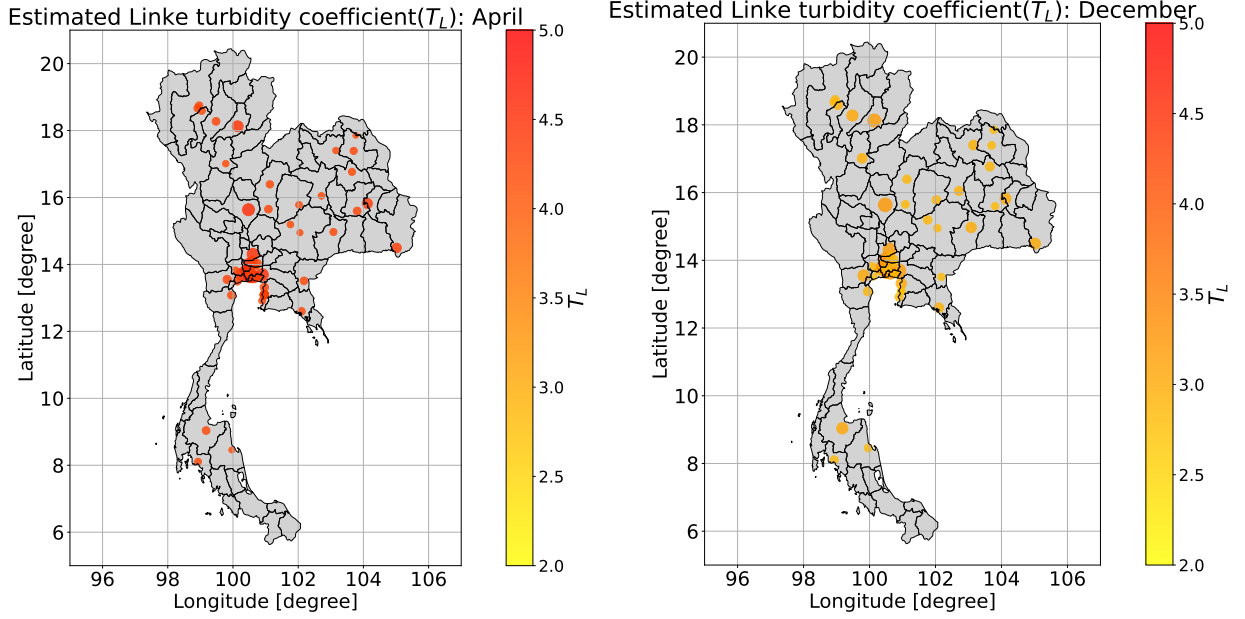
$$f_{h_1} = e^{-h/8000}, f_{h_2} = e^{-h/1250}, a_1 = 5.09 \times 10^{-5}h + 0.868, a_2 = 3.92 \times 10^{-5}h + 0.0387,$$

where h is retrieved from STRM30 dataset [MC00]. We follow the model of air mass coefficient, $\text{AM}(t)$, from [PPGB13] given by

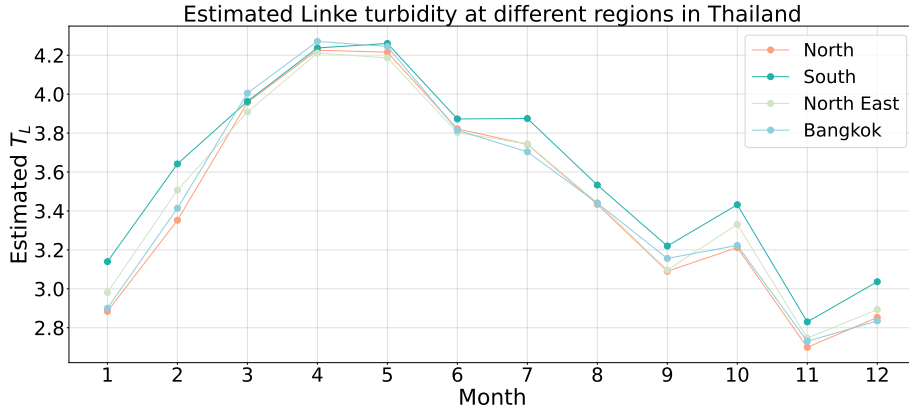
$$\text{AM}(t) = \frac{1}{\cos \theta(t) + 0.50572(96.07995 - \theta(t))^{-1.6364}}. \quad (3)$$

The Linke turbidity parameter T_L represents the amount of atmospheric absorption by water vapor and aerosol particles that attenuate extraterrestrial radiation. This factor can be obtained via experiments on clear-sky days. Still, it is more common to be empirically estimated [ERA⁺12], where T_L is empirically estimated to best match with local ground measurement of clear-sky irradiance in Thailand.

We have set up an experiment to adjust the Linke turbidity coefficients based on ground measurements of GHI from 53-station data. The clear-sky GHI portions are extracted from PVlib clear-sky detection implementation [AHH⁺23] and split into train:test at ratio 90:10. The training set is divided into 12 months and monthly T_L coefficients are estimated separately since the value T_L is known to vary seasonally [Ine08b, GL23]. The estimation technique is nonlinear regression to fit the clear-sky GHI curves. Figure 5b shows the result of estimated T_L as a heatmap displaying the value across the Thailand map, where its value is high during April but appears lower in December. A complete trend of T_L estimated monthly is shown in Figure 5c. The coefficient T_L is at peak during Apr-May and smaller in other months.



(a) Estimated coefficients T_L of April across 53 locations. (b) Estimated coefficients T_L of December across 53 locations.



(c) Estimated coefficients T_L across 12 months.

Figure 5: Results of Linke turbidity coefficients (T_L) estimation of 12-month data.

Other guidelines of T_L estimation in Thailand can be found in [JKL03, CC04]. Other papers about the Linke estimation are presented in [Ine08b, GL23].

3.2 Satellite-derived GHI estimation

The estimation of GHI based on satellite-derived information has two schemes explained in Section 1. The physics-based and semi-empirical methods are typically based on the top diagram in Figure 6. The cloud index extracted from satellite images is an input for an irradiance attenuation model that produces an estimate of clear-sky index. Examples in literature are Heliosat algorithms [RLW04, QOB⁺17], piece-wise polynomial and rational functions [SWH⁺24]. The estimated \hat{k} is then used for compensating a reduction in irradiance through the relationship $\hat{I} = \hat{k} \cdot I_{\text{clr}}$.

Instead of expressing the effect of the cloud on the clear-sky index directly, we propose to use a nonlinear mapping as **GHI estimation model** to associate cloud index, clear-sky GHI, and other features with the estimate GHI, as shown in the bottom diagram of Figure 6. The non-linear map can better capture complex cloud effects on solar irradiance, and various choices of GHI estimation model can be considered, *e.g.*, tree-based models were validated with a good MAE/RMSE performance in [SWH⁺24]. Note that the input features for the non-linear mapping are all meteorological variables, especially the cloud index, but not GHI measurements as they are not available spatially across Thailand when deploying the model in practice. The list of features we used in this paper are

$$CI_M, CI_R, I_{\text{clr}}, I_{\text{nwp}}, T_{\text{nwp}}, \text{lat}, \text{long}, \text{hour}, \text{day}$$

Let $x(t) := \{CI_M, CI_R, I_{\text{clr}}, I_{\text{nwp}}, T_{\text{nwp}}, \text{lat}, \text{long}, \text{hour}, \text{day}\}$ denotes a vector collecting these input features at time t .

Table 1: Benchmarked GHI estimation models.

Model	Description
LGBM	max_depth = 15, p=5, num_leaves = 31, num_iter = 500, learning_rate = 0.1
LSTM	L=1, p=5, hidden=128, Dropout=0.001, learning_rate = 0.001
Informer	L=2, p=5, hidden=16, Dropout=0.001, learning_rate = 0.001
Transformer	L=2, p=5, hidden=64, Dropout=0.001, learning_rate = 0.001

Then, the input sequence X is the collection of the input $x(t)$ and its lags, *i.e.*,

$$X = [x(t), x(t-1), \dots, x(t-p)]$$

where p is the length of input sequence. Suppose that $f_{\Theta}(\cdot)$ is a GHI estimation model that is data-driven with tuned parameters Θ . The GHI estimate at time t can be obtained by performing the model inference: $\hat{I}(t) = f(X; \Theta)$.

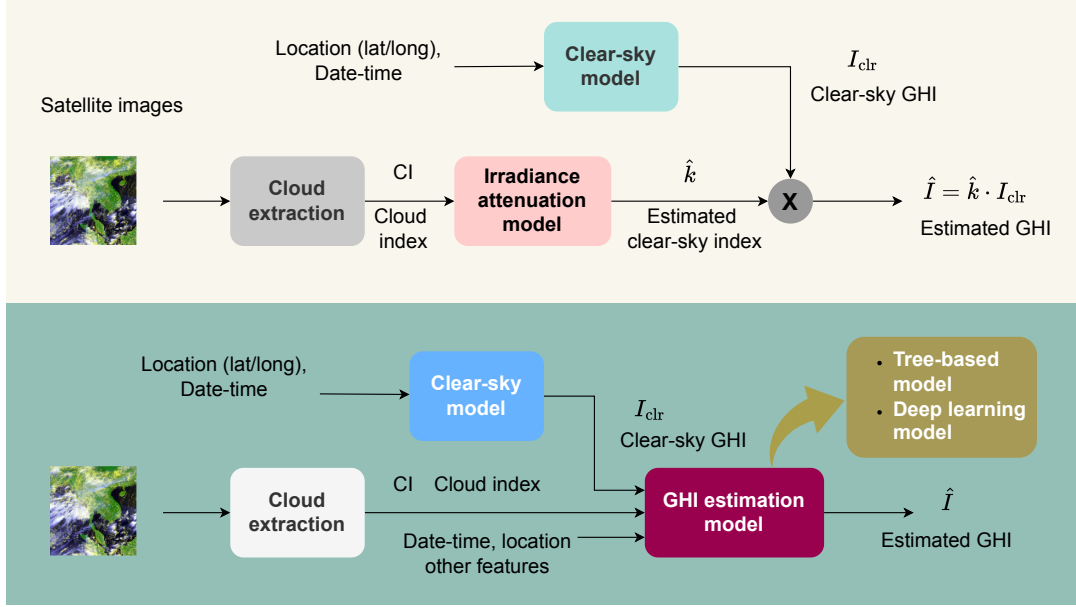


Figure 6: GHI estimation schemes: (*Top.*) Physic-based or empirical method. (*Bottom.*) Proposed scheme.

When training a model, it is natural to enforce the similarity between the prediction $\hat{I}(t)$ and the ground truth $I(t)$. In this study, we benchmark the following methods: **LightGBM (LGBM)**, **LSTM**, **Informer**, **Transformer**, and **the service X**. For service X’s predictions, we have downloaded historical GHI estimates at 53 stations during the period of this study. We modified Transformer and Informer to acquire time-series data for solar irradiance forecasting while building upon existing LSTMs with additional linear layers. The hyper-parameters of these models were tuned and set with the values shown in Table 1.

3.2.1 LightGBM

LightGBM [KMF⁺17] (light gradient boosted machine) builds on the concept of gradient boosting decision trees. LightGBM uses the leaf-wise approach that prioritizes growing trees in informative areas, leading to more accurate models with fewer trees. Also, it has a process to select important features and remove less impactful features from the data. In our case, we provide the following features as the input to the LightGBM:

$$CI_M(t-p), \dots, CI_M(t), CI_R(t-p), \dots, CI_R(t), I_{clr}, I_{nwp}, T_{nwp}, \text{lat, long, hour, day}$$

The parameter setting of LightGBM is provided in Table 1.

3.2.2 LSTM

Our LSTM (long short-term memory) neural network is enhanced from that of [SL18] to include L layers of LSTM cells, an activation, a dropout, and a linear layer, as shown in Figure 7a, where $X \in \mathbf{R}^{p \times d}$ is fed as the input, and the predicted irradiance $\hat{I}(t) \in \mathbf{R}$ is the output. The LSTM cell is provided in Figure 7b. Its cell state and hidden state are initialized at zero. The LSTM cell recursively processes each input lag from X . For an input $x(t-p)$, the long-term memory $c_l(t-p)$ is updated from the previous $c_l(t-p-1)$ and the forget gate $f(t-p)$. The short-term memory $c_s(t-p)$ is updated

with the input gate $i(t-p)$ and $g(t-p)$. The output gate provides the output $o(t-p)$ and is used to update next hidden state $h(t-p)$. After each recursion, the output is collected as a latent sequence $o(t-p), \dots, o(t)$, fed to Relu activation, dropout layer, and linear layer. The linear layer maps the output sequence into a sequence of GHI estimates $\hat{I}(t-p), \dots, \hat{I}(t)$, where the last element is the prediction $\hat{I}(t)$.

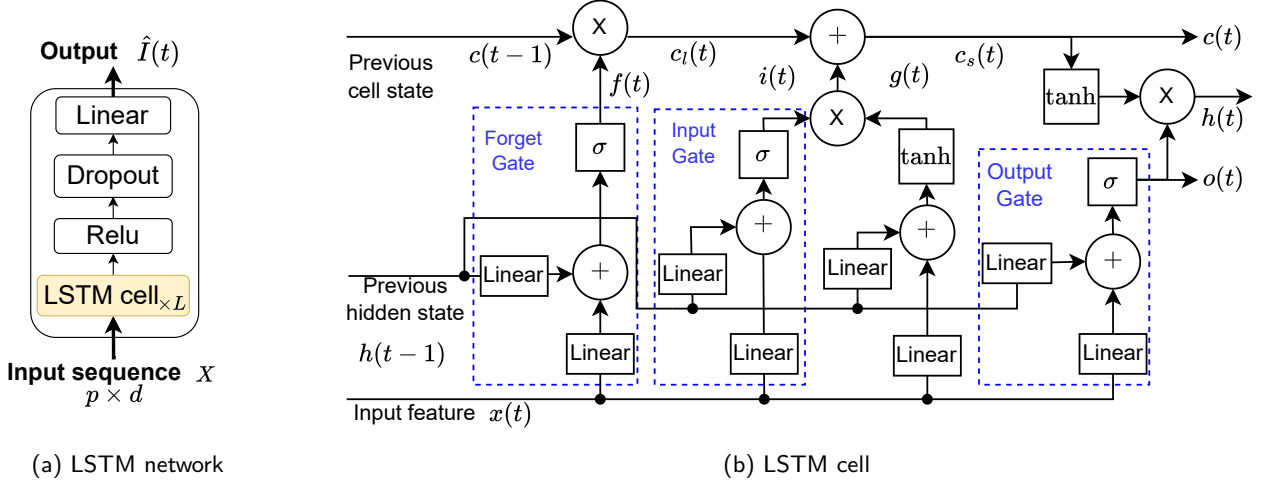


Figure 7: (a) LSTM network and (b) LSTM cell.

3.2.3 Transformer

We modify the Transformer [VSP⁺17] by, *first*, applying the attention mechanism to capture the dependencies within a time-series sequence and between the pairs of such sequences. *Second*, the architecture is modified for the shorter sequence, resulting in the encoder-decoder pairs shown in Figure 8a, which is similar to [ZZP⁺20], except that our input features and target priors are not the target itself. At first, the encoder receives the input sequence X , which calculates the self-attention to capture the dependencies within the sequence itself. Three linear layers (Linear) encode X as Q , K , and V in $\mathbf{R}^{p \times d}$. The self-attention mechanism can be expressed as follows (and in Figure 8b):

$$\text{Atten}(Q, K, V) = \text{Softmax}\left(\frac{QK^T}{\sqrt{d}}\right)V \quad (4)$$

The decoder derives the prediction from cross-attention between target priors (T_{prior}) and the latent features from encoder. The target priors are the sequence of the following features:

$$T_{prior} = \{I_{clr}, \text{lat}, \text{long}, \text{hour}, \text{month}, \text{day}, I_{nwp}, T_{nwp}\} \quad (5)$$

which are used as the query in the attention calculation. The latent features from the encoder are the key-value pair.

3.2.4 Informer

The architecture of Informer [ZZP⁺20] is similar to that of Transformer, except that the generic attention mechanism is replaced with the sparse attention mechanism [LZC⁺23, ZZP⁺20]. We further modify Informer for predicting the solar irradiance $\hat{I}(t)$ by adding the target priors as 5. At first, the score of the queries' sparsity is calculated, and then only the top- u queries with the highest scores are selected to construct a sparse query matrix. Thus, we can construct a sparse query matrix (denoted as \bar{Q}) that contains only the top- u highest sparsity scores. The sparse attention mechanism can be formulated by replacing Q with \bar{Q} in Equation (4), *i.e.*,

$$\text{SparseAtten}(Q, K, V) = \text{Softmax}\left(\frac{\bar{Q}K^T}{\sqrt{d_k}}\right)V \quad (6)$$

Figure 8c shows the sparse attention mechanism.

4 Results and discussion

4.1 Data preparation

Since cloud cover can vary greatly throughout the day, traditional seasonal patterns become less reliable. It is important to ensure that the data samples in the training, validation, and test datasets share a similar degree of uncertainty. We

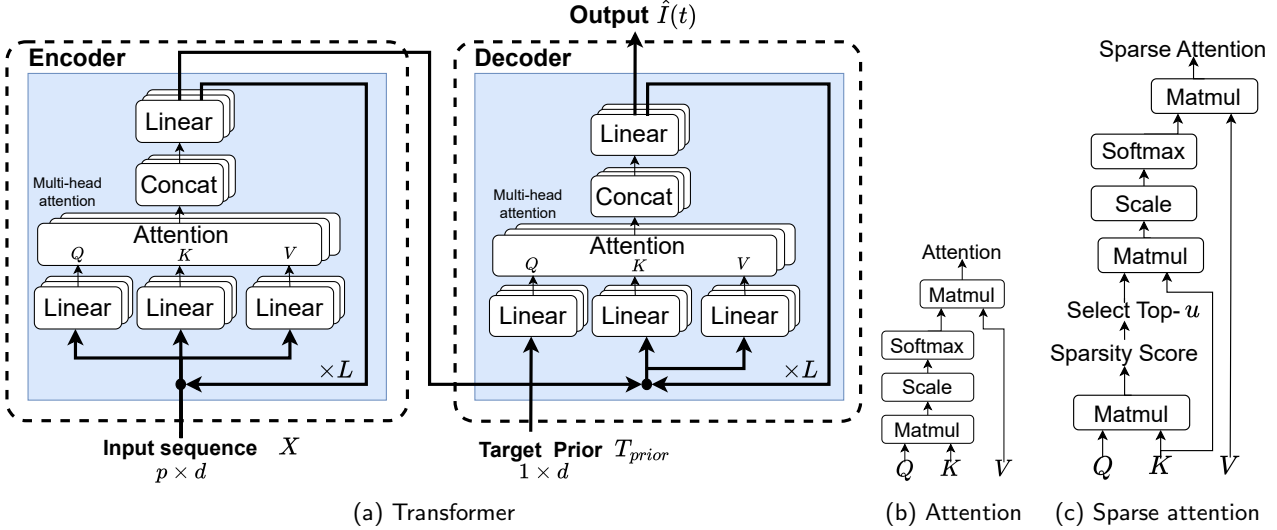


Figure 8: (a) Transformer architecture, (b) attention mechanism, and (c) sparse attention mechanism.

classify GHI data of each day into three sky conditions: clear, partly cloudy, and cloudy, according to the rate of change in GHI and the daily average of clear-sky index $k(t)$, or \bar{k} . If the GHI curve has a smooth clear-sky curve, its slope must decrease (change from a positive value to zero and a negative value); meanwhile, the higher \bar{k} indicates the lower cloud coverage. The criteria of our classification are described as follows: i) *clear-sky*: GHI curve has decreasing slope, and $\bar{k} \geq 0.6$, ii) *partly-cloudy*: GHI curve that are not clear-sky, and $\bar{k} \geq 0.6$, and iii) *cloudy*: GHI curve that are not clear-sky, and $\bar{k} < 0.6$.

The extracted cloud index and ground GHI data are merged into a synchronized 15-min resolution during 03:00-17:00 (local time in Thailand), totaling 1,195,257 samples or 20,924 days. The target forecasting hours range from 7:00 to 17:00. The data is divided with the ratio of 60:20:20 for train:validation:test, where each of the three sets is ensured to contain a uniform mix of three sky conditions see Table 2. To achieve this, we first segmented the data with lags and stacked them as sequences labeled with sky condition. Then, we shuffle the data and split them for training, validation, and testing.

Table 2: Data split under sky conditions and data samples in train, validation, and test sets.

Sky condition	Total days	Total samples	Train	Validation	Test
clear-sky	921	49,038	28,979	10,907	9,152
partly-cloudy	21,549	1,123,391	675,227	224,739	223,425
cloudy	436	22,828	14,140	4,426	4,262
Total	22,906	1,195,257	718,346	240,072	236,839

4.2 Clear-sky model evaluation

According to our improvement of the Ineichen clear-sky model in Section 3.1, we benchmark the results against the following methods.

1. Ineichen model with T_L updated using clear-sky GHI measurements (proposed).
2. Ineichen model computed by PVlib [AHH⁺23].
3. Simplified Solis model computed by PVlib [AHH⁺23].
4. Pysolar [Sta14]. The library does not provide GHI but only returns DNI, so we multiply DNI with $\cos\theta(t)$.

Figure 9 shows that after we tuned T_L to local GHI data in Thailand, the Ineichen clear-sky model fits better to clear-sky time series while other methods tend to be overestimated (on selected sample dates in Figure 9. The MBE in Figure 10 (b) clearly shows that PVlib Ineichen and PySolar highly underestimate clear-sky GHI during Jun-Sep, while PVlib simplified Solis overestimates during Feb-May. Our method achieves the least MAE and MBE in all months.

4.3 Satellite-derived GHI estimation

Figure 11 and Table 3 show a comparative performance of all GHI estimation models, including LGBM, LSTM, Informer, Transformer, and the service X. All the proposed benchmarked models provide similar overall MAEs in the range of 78-81

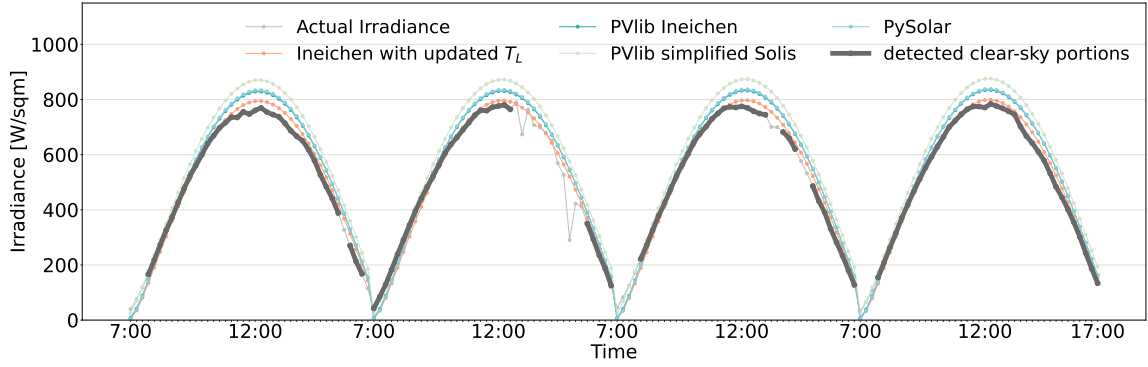


Figure 9: GHI time series that are detected as clear-sky (thick gray portions.)

W/m^2 . For the MAE, the Informer, Transformer, and service X have the lowest error in clear-sky, partly cloudy, and cloudy conditions, respectively. For the MBE, LGBM and the service X have a relatively high negative bias (underestimate) in clear and partly cloudy condition. Meanwhile, LSTM, Informer, and Transformer tend to overestimate—high positive bias in the cloudy condition, while the service X has the lowest MBE in this case, as shown in Figure 11 (*Bottom*.) The evaluation with the RMSE metric is reported in Table 3. All the proposed models perform almost equally if MAE is considered. For specific sky conditions, our proposed models generally perform well in clear-sky and partly cloudy scenarios. However, service X demonstrates superior performance under cloudy conditions.

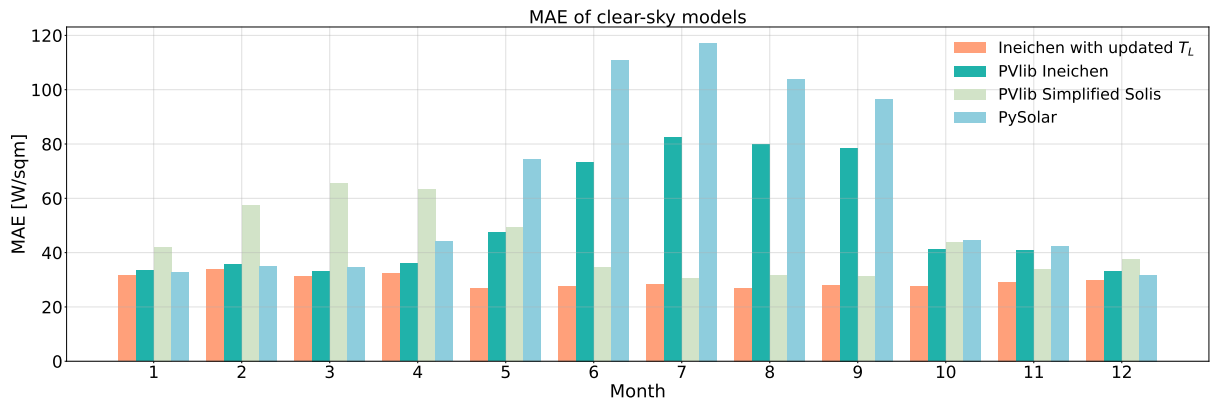
Table 3: Model comparison of performance metrics: MAE, RMSE, and MBE (W/m^2) under three sky conditions.

Model	LGBM	LSTM	Informer	Transformer	Service X
MAE (W/m^2)					
Overall MAE	78.58	80.41	78.97	78.52	80.80
Clear sky	19.73	18.92	17.99	18.11	27.00
Partly cloudy	75.93	77.62	76.30	75.90	80.16
Cloudy	97.01	99.68	97.81	97.07	91.99
RMSE (W/m^2)					
Overall RMSE	118.97	125.86	124.54	123.82	121.99
Clear sky	36.70	32.79	31.54	31.94	39.52
Partly cloudy	115.13	122.19	121.21	120.58	120.58
Cloudy	138.53	145.74	143.45	142.42	135.01
MBE (W/m^2)					
Overall MBE	-0.47	6.11	4.55	5.59	-4.21
Clear sky	-7.86	-1.24	-1.86	-1.71	-5.62
Partly cloudy	-7.48	2.04	0.53	2.09	-6.17
Cloudy	23.07	20.29	18.41	17.97	2.26

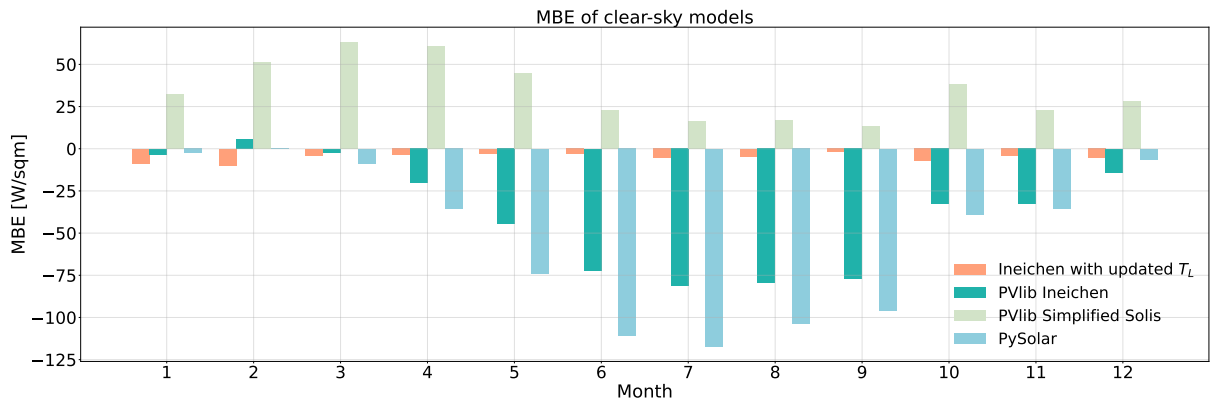
Comparison with literature Our GHI estimation at a half-hourly resolution provides the RMSE values ($31.54 - 145.74 W/m^2$) that aligns with previous studies in equatorial regions, *i.e.*, [VPN⁺23] reported hourly GHI RMSEs of $115-180W/m^2$ across six locations (SAP, TAT, FUA, ISH, DWN, and ASP) using Himawari-8 data; and, [QHM⁺21] reported an instantaneous GHI RMSE of $118.3 W/m^2$ at the DWN station, also using Himawari-8. Our results are in a similar trend to [KBSH18], providing half-hourly GHI RMSEs of $41.7-167 W/m^2$ in South Asia (India). [Bri19] reported an average hourly RMSE of $99.5 W/m^2$ in equatorial regions for zenith angles between 0 and 85 degrees (*approx.* 05:56-18:37), exceeding our target forecasting hours (7:00-17:00). Note that including GHI estimates from early morning and late evening (nearly night-time) in the analysis could potentially underestimate the MAE and RMSE.

Impact of selected features We explore possibly different characteristics of models when some features are not included in the model. NWP forecasts (both irradiance and temperature) are the input that is likely to be costly in operational setting when inferring a solar map of Thailand since the forecast values must be obtained a high spatial resolution. The coordinates of station locations are also considered to be removed, as this information is already inherited in the clear-sky model. Table 4 shows that dropping NWP input affects the performance slightly for all models and all-sky conditions, while the location coordinate still has some significance as the MAE is increased around $2 W/m^2$. The Informer has the least MAE among all models when all two features are removed. Thus, we will focus on the performance of the informer.

The solar irradiance estimation by Informer is provided in Figure 12. The discrepancies between the estimates and ground truth appear to be larger when the sky is cloudy, as shown in Figure 12 (a). Meanwhile, the MAE evaluated for each hour of the day indicates that the model usually suffers during the daytime (10:00-15:00) under the presence of



(a) MAE of clear-sky GHI.



(b) MBE of clear-sky GHI.

Figure 10: Validated results of clear-sky models with clear-sky measurements.

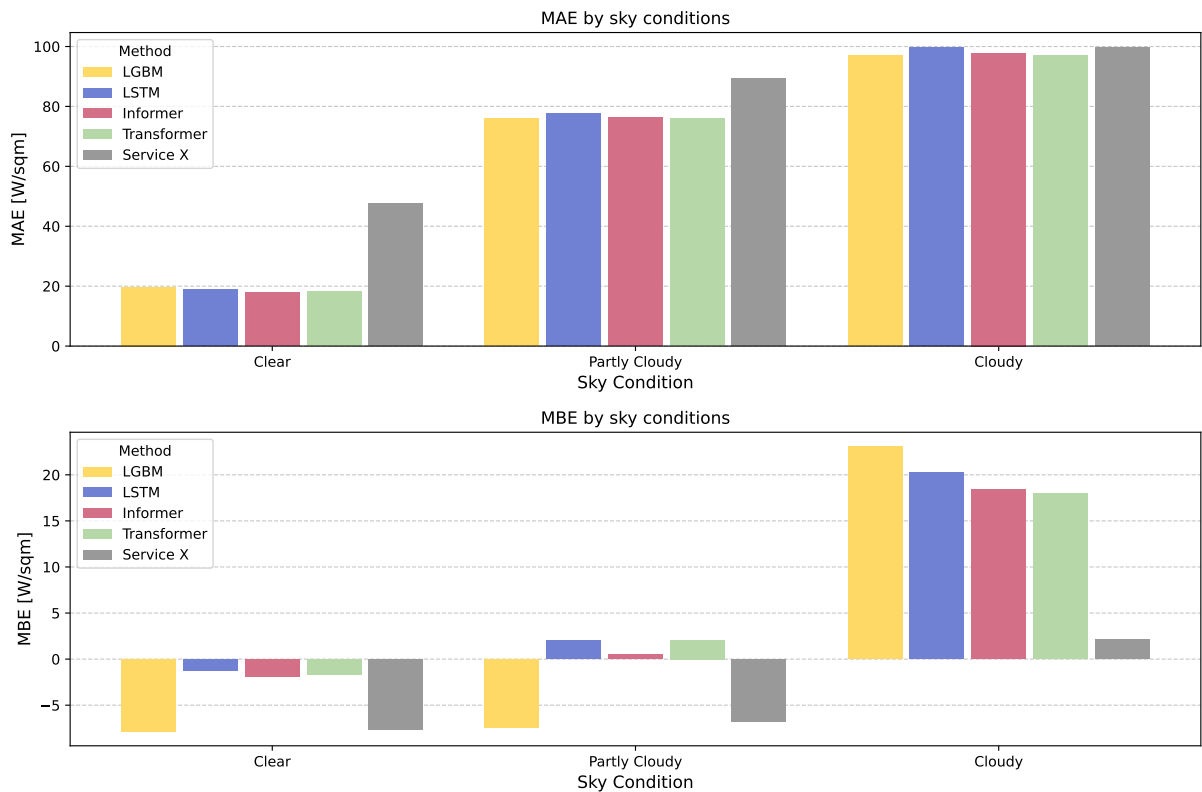


Figure 11: Satellite-derived GHI estimation from benchmarked models: (Top.) Validated MAE. (Bottom.) MBE

Table 4: MAE comparison (W/m^2) when some features are removed.

Model	LGBM	LSTM	Informer	Transformer
Overall				
all features	78.58	80.41	78.97	78.52
no NWP	78.98	80.77	78.67	79.06
no NWP + Lat/Long	82.35	82.05	80.85	80.98
Clear sky				
all features	19.73	18.92	17.99	18.11
no NWP	20.41	20.11	17.90	18.75
no NWP + Lat/Long	24.38	22.21	21.15	21.93
Partly cloudy				
all features	75.93	77.62	76.30	75.90
no NWP	76.27	77.86	75.74	76.38
no NWP + Lat/Long	79.97	79.50	78.29	78.36
Cloudy				
all features	97.01	99.68	97.81	97.07
no NWP	97.56	100.31	98.30	97.80
no NWP + Lat/Long	99.76	100.51	99.12	99.31

cloud, as shown in Figure 12 (b). The MAE could go up to $140 W/m^2$ in this period, and the positive MBE explains that the model mostly overestimates in this period. Figure 12 (c) and (d) show the selected time series with the top three lowest and highest daily average MAE, respectively. The time series with the lowest error often co-occurs with the clear sky condition, where the cloud index is relatively low. The time series with the highest error typically happens with cloud fluctuation during the day. Thus, the model functioned as expected; if CI increases, the estimate \hat{I} decreases. A high estimation error, for example, the middle of the plot (d), could come from approximation in the data processing step. It could be the case that CI was missing before 14:00, and the displayed values were interpolated (as a constant of 0.3 from backward imputation).

4.4 Solar energy in Thailand

Estimated GHI across Thailand by Informer are cumulatively summed up in yearly, monthly, and hourly time scales of 2023 to infer a solar energy map of Thailand shown in Figure 13.

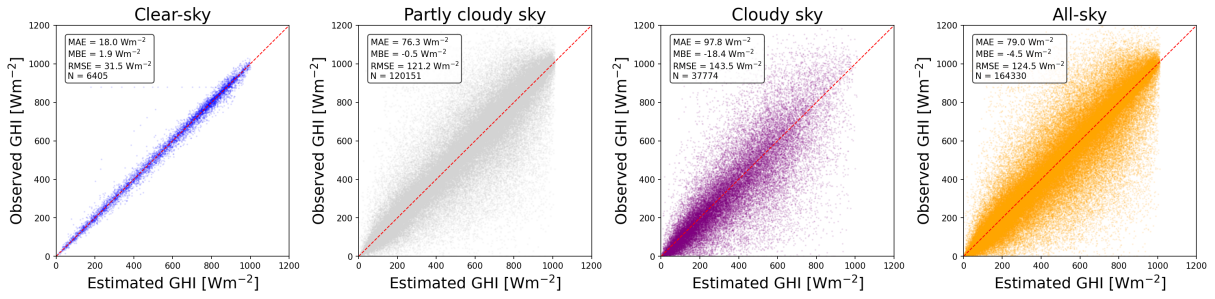
We compare our results with previous studies that visualized solar energy maps in nearby countries. Ministry of Energy, Thailand, currently has developed a yearly solar energy map [Mas22, JMPL13] using long-term data from GMS-5, GOES-9, MTSAT, and Himawari satellites. The methodology relied on physical and semi-empirical models presented in [JMPL13] that require reflectivity and absorption by water vapor, ozone, and particles to infer global solar radiation. [JLS11] presented an application for investigating potential areas in Thailand for producing electricity from solar power. The method used GMS5 satellite data from 1995-2002, where the variables include reflectivity and absorption by water vapor, which was computed by ambient temperature and relative humidity. The map presented the year sum of DNI. [RAN12] visualized monthly solar energy in Indonesia using estimates from an ANN model with weather inputs and geographical information. [SS16] used the historical MERRA solar radiation dataset to analyze potential solar power areas in Southeast Asia. Eastern Thailand, Java, and central Myanmar were the best locations for solar power use.

Figure 13a shows total yearly energy where effective areas yielding high solar energy lie in central and northeastern regions; the result aligns with that of the solar radiation map provided by DeDe (https://gis.dede.go.th/upload/20230302_135735.pdf); see the Appendix. Figure 13b shows the monthly estimated energy, with most of Thailand experiencing the highest levels of $170-180 kWh/m^2$ in March, April, and May. This aligns with the monthly average of daily global radiation in 2013 [JMPL13], which peaks at approximately $183 kWh/m^2$ or $22 MJ/m^2$ – day during the same months. However, due to missing data (52% in July and 67% in November), the monthly GHI estimates for these months are extrapolated, resulting in a solar map that differs from [JMPL13].

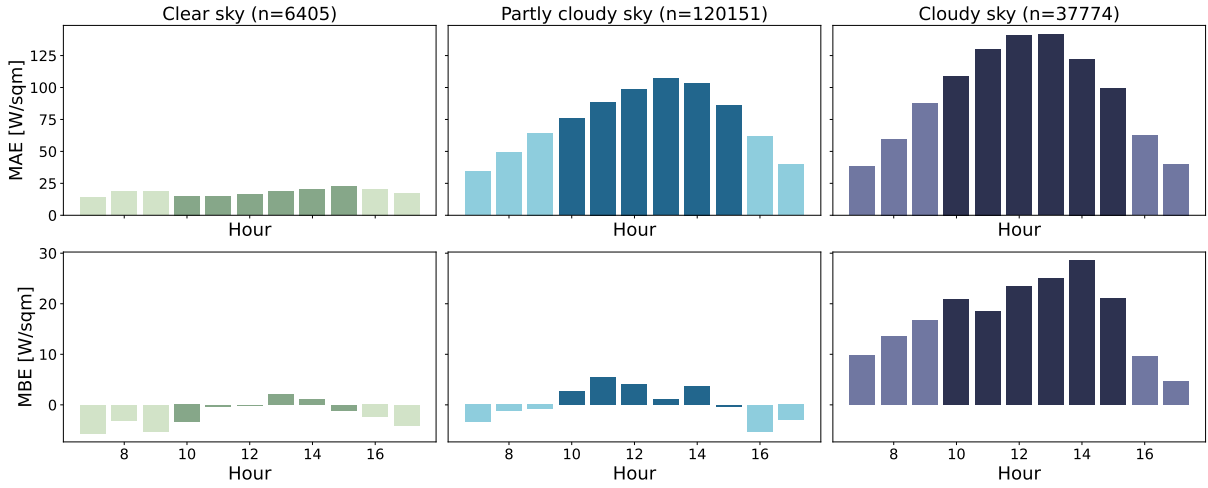
Figure 13c illustrates hourly-updated GHI estimates on June 15, 2023. Our GHI estimation model can provide solar energy estimation at the finer temporal resolution, compared to [JMPL13], which was aimed at analyzing a monthly resolution. Our model prioritizes near real-time updates, which offers a significant advantage for operational settings in energy applications where real-time updates are crucial.

4.5 Deployment and runtime

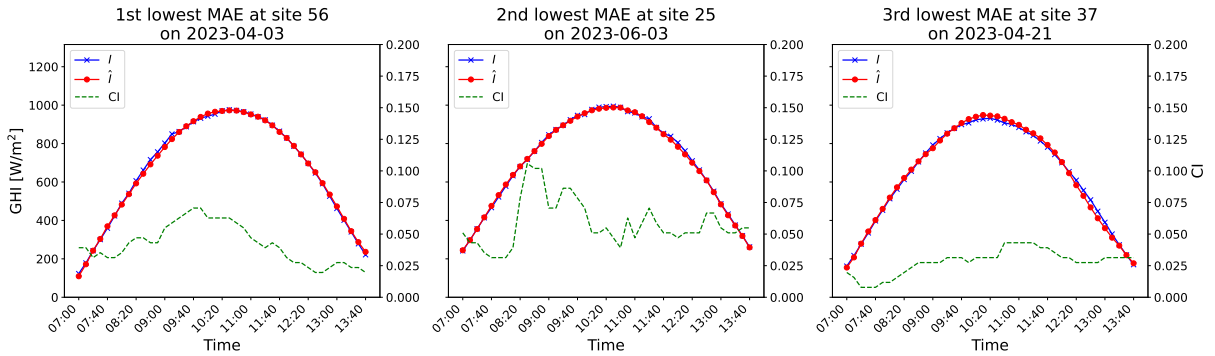
Our GHI models are deployed to provide the solar map at two spatial resolutions: zoom level 12 (6,843 grids, approximately $\approx 9.8 \times 9.8 km^2$ per grid) and zoom level 14 (93,061 grids, approximately $\approx 2.5 \times 2.5 km^2$ per grid). To efficiently estimate solar irradiance for all grid points simultaneously, we set the batch size equal to the total number of grids in each map. The runtime performance of LSTM, Informer, and Transformer models on an RTX4060 GPU for this process is presented in Table 5. From Section 3.2.1, when directly including latitude and longitude as features for LGBM, the generated solar map displays some abrupt changes in estimated GHI at some region boundary. These unrealistic results can be fixed



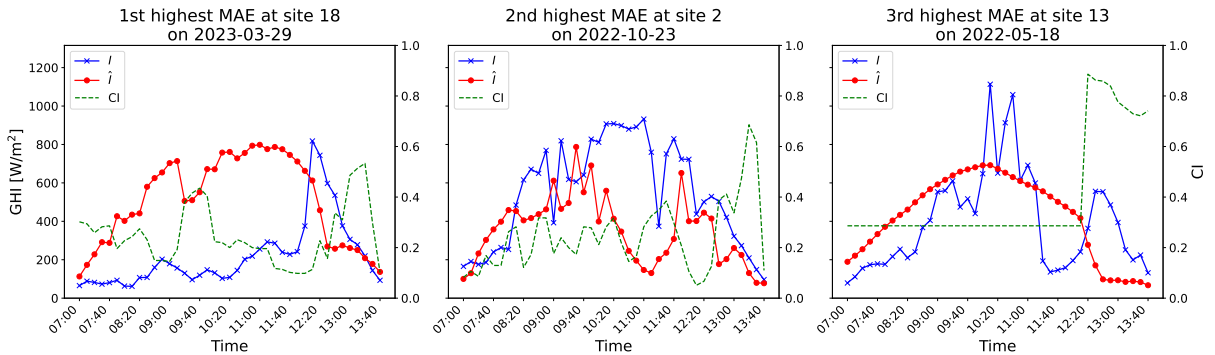
(a) Scatter plot between the estimated and actual irradiance.



(b) MAE and MBE across three sky conditions and hours of day.



(c) Three lowest MAE.



(d) Three highest MAE.

Figure 12: Solar irradiance estimation by Informer: (a) Discrepancy against the actual irradiance and (b) MAE and MBE across three sky conditions and hours of the day. The samples of the selected time series with (d) the top three lowest and (e) the top three highest daily average MAE.

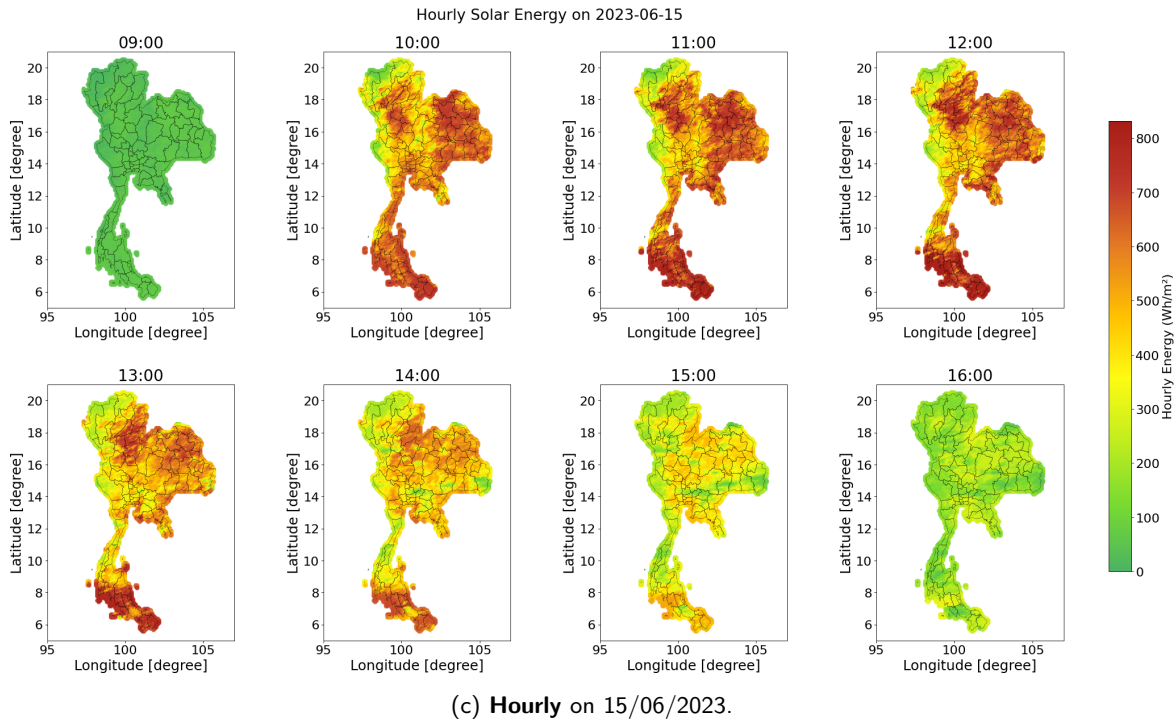
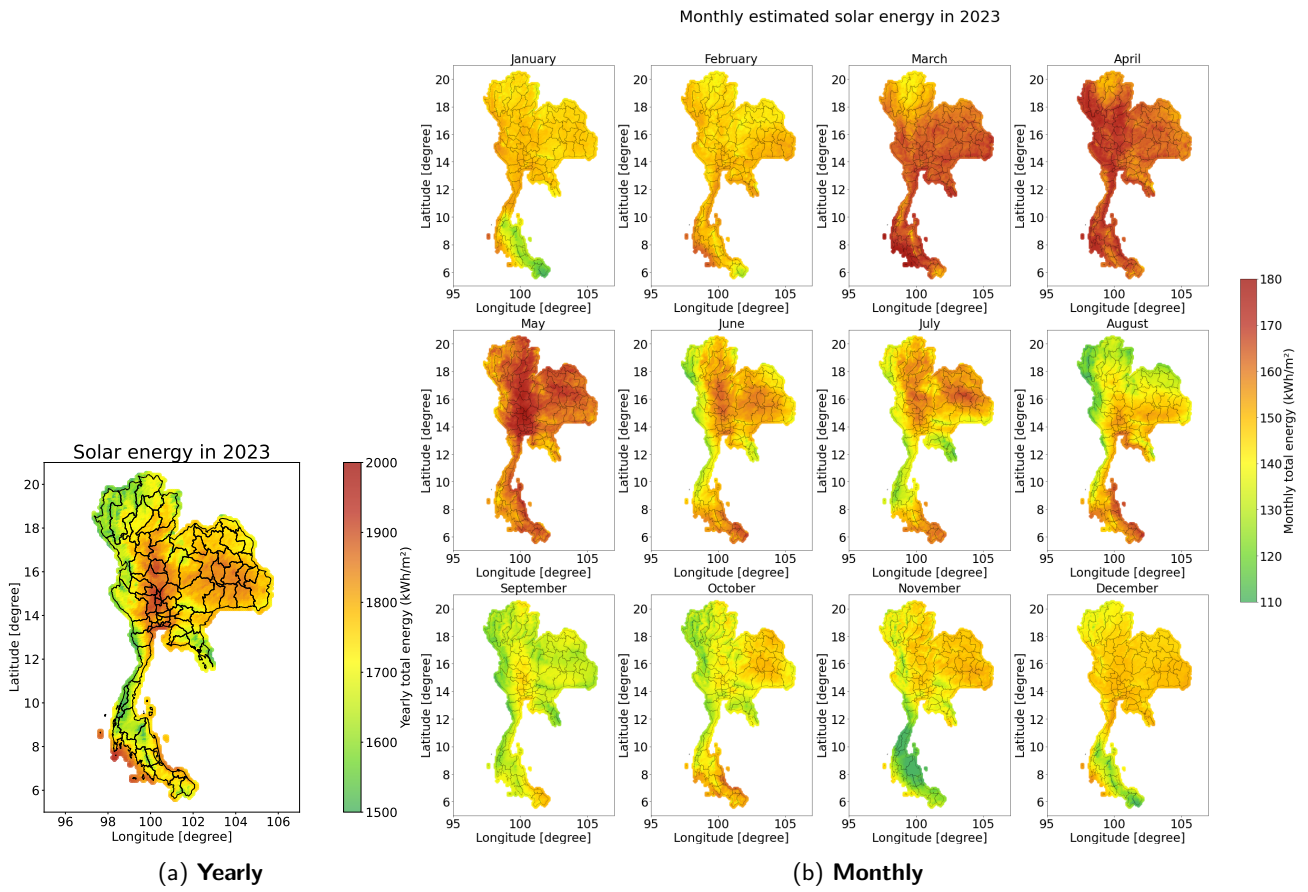


Figure 13: Estimated total solar energy in 2023, Thailand, by the Informer model.

when removing these two features, with the cost of having 2-3 W/m² MAE increased. For this reason, LGBM results are excluded from the runtime report. All models show acceptable performance (≤ 2 secs. for the largest batch size), with LSTM being the fastest. The Transformer can be an alternative to the Informer because of their similar performance.

Table 5: Average performance per run: inference runtime, overall runtime (inference + data loading), and peak memory.

	DL models	Inference (ms)	Overall (ms)	Peak memory (MB)
Zoom level 12 (Batch size = 6,843)	LSTM	22.35	123.89	417.86
	Informer	72.29	151.47	581.50
	Transformer	67.83	151.70	583.69
Zoom level 14 (Batch size = 93,601)	LSTM	307.43	1,757.57	5,451.18
	Informer	561.87	1,999.29	7,754.21
	Transformer	500.84	1,946.88	7,783.98

5 Conclusions

This research presented a methodology of a satellite-derived GHI estimation across Thailand with a spatial resolution of $2.4 \times 2.4 \text{ km}^2$, totaling 93,061 grids with 30-minute updates using cloud indices extracted from Himawari-8 satellite imageries, along with the output of Ineichen and Perez’s clear-sky irradiance model as main features of our GHI estimation models. The study explored recently effective machine learning models, including LightGBM (LGBM), LSTM, Informer, and Transformer, to capture complex cloud effects on ground irradiance attenuation. To optimize computational efficiency, input data is processed as time series, with necessary modifications to the Informer and Transformer. Benchmarking against a commercial service from 53 ground stations demonstrates an improved performance, with lower MAE and RMSE values. Our GHI estimates, at a half-hourly resolution and with RMSE values ranging from 31.54 to 142.42 W/m^2 , align with previous studies [KBSH18, Bri19, QHM⁺21, VPN⁺23]. We provide real-time solar energy maps at hourly, monthly, and yearly resolutions, and assess computational efficiency at different spatial scales. Our monthly results on March, April, and May are aligned with the monthly average of daily global irradiance in 2013 during the same months [JMPL13]. Additionally, we confirmed the feasibility of using these models for real-time GHI estimation at the required temporal resolution.

6 Acknowledgment

The authors thank Parinthorn Manomaisaowapak for developing the GHI estimation model (version-2), Justin Jirratsakul and NDR solution (Thailand) Co., Ltd. for implementing the solar map platform as well as Tanan Boonyasirikul for the initial experiments on the DL models. We appreciate the discussions with the Division of Solar Energy Development, Department of Alternative Energy Development and Efficiency (DeDe), Ministry of Energy, which provided supplementary solar data and a historical yearly solar map. This work was co-funded by the Chula Engineering Research grant 2023 and partially supported by Grants for Development of New Faculty Staff, Ratchadaphiseksomphot Endowment Fund.

References

- [So24] Soda-Pro . Solar radiation and meteorological data services to optimize solar energy production toward a sustainable future, 2024.
- [AHH⁺23] Kevin S Anderson, Clifford W Hansen, William F Holmgren, Adam R Jensen, Mark A Mikofski, and Anton Driesse. pvlb python: 2023 project update. *Journal of Open Source Software*, 8(92):5994, 2023.
- [AMOG14] Mohammad H. Alobaidi, Prashanth R. Marpu, Taha B. M. J. Ouarda, and Hosni Ghedira. Mapping of the solar irradiance in the UAE using advanced artificial neural network ensemble. *IEEE Journal of Selected Topics in Applied Earth Observations and Remote Sensing*, 7:3668–3680, 8 2014.
- [AMR21] Meenu Ajith and Manel Martínez-Ramón. Deep learning based solar radiation micro forecast by fusion of infrared cloud images and radiation data. *Applied Energy*, 294:117014, 7 2021.
- [BBZ⁺20] Jamie M. Bright, Xinyu Bai, Yue Zhang, Xixi Sun, Brendan Acord, and Peng Wang. irrady: Python package for MERRA-2 download, extraction and usage for clear-sky irradiance modelling. *Solar Energy*, 199:685–693, 3 2020.
- [Bri19] Jamie M. Bright. Solcast: validation of a satellite-derived solar irradiance dataset. *Solar Energy*, 189:435–449, 9 2019.
- [BS21] Jamie M. Bright and Xixi Sun. Statistical satellite-derived irradiance estimation: A case study in Singapore. In *2021 IEEE 48th Photovoltaic Specialists Conference (PVSC)*, pages 0835–0842. IEEE, 6 2021.
- [CC04] Pipat Chaiwiwatworakul and Surapong Chirattananon. An investigation of atmospheric turbidity of thai sky. *Energy and Buildings*, 36:650–659, 7 2004.

- [Dag05] Knut-Frode Dagestad. *Estimating global radiation at ground level from satellite images*. PhD thesis, Bergen University, 2005.
- [Dep15] Department of Alternative Energy Development and Efficiency, Ministry of Energy, Thailand. *Alternative energy development plan: 2015 – 2036 (aedp 2015)*, 2015.
- [Dob13] Aron P. Dobos. *PVWatts version 1 technical reference*, 2013.
- [Ene21] Energy Policy and Planning Office, Ministry of Energy, Thailand. *National energy plan, 2021*. Accessed: 2024-7-31.
- [Ene24] Energy Policy and Planning Office, Ministry of Energy, Thailand. *Draft of power development plan 2024-2037 (pdp 2024) for public hearing*, 2024.
- [ERA⁺12] Yousef A. Eltbaakh, M.H. Ruslan, M.A. Alghoul, M.Y. Othman, K. Sopian, and T.M. Razykov. Solar attenuation by aerosols: An overview. *Renewable and Sustainable Energy Reviews*, 16:4264–4276, 8 2012.
- [FZ20] Cong Feng and Jie Zhang. SolarNet: A sky image-based deep convolutional neural network for intra-hour solar forecasting. *Solar Energy*, 116:103098, 2 2020.
- [GBL⁺19] Christian A. Gueymard, Jamie M. Bright, David Lingfors, Aron Habte, and Manajit Sengupta. A posteriori clear-sky identification methods in solar irradiance time series: Review and preliminary validation using sky imagers. *Renewable and Sustainable Energy Reviews*, 109:412–427, 7 2019.
- [GCM⁺22] R. Gallo, M. Castangia, A. Macii, E. Macii, E. Patti, and A. Aliberti. Solar radiation forecasting with deep learning techniques integrating geostationary satellite images. *Engineering Applications of Artificial Intelligence*, 116:105493, 2022.
- [GL23] Pranda M.P. Garniwa and Hyunjin Lee. Intercomparison of the parameterized Linke turbidity factor in deriving global horizontal irradiance. *Renewable Energy*, 212:285–298, 8 2023.
- [HV22] Jen-Yu Han and Petr Vohnicky. An optimized approach for mapping solar irradiance in a mid-low latitude region based on a site-adaptation technique using Himawari-8 satellite imageries. *Renewable Energy*, 187:603–617, 3 2022.
- [Ine08a] Pierre Ineichen. A broadband simplified version of the solis clear sky model. *Solar Energy*, 82:758–762, 8 2008.
- [Ine08b] Pierre Ineichen. Conversion function between the Linke turbidity and the atmospheric water vapor and aerosol content. *Solar Energy*, 82:1095–1097, 11 2008.
- [IP02] Pierre Ineichen and Richard Perez. A new air mass independent formulation for the Linke turbidity coefficient. *Solar Energy*, 73:151–157, 9 2002.
- [JKL03] S. Janjai, W. Kumharn, and J. Laksanaboonsong. Determination of angstrom's turbidity coefficient over thailand. *Renewable Energy*, 28:1685–1700, 9 2003.
- [JLQ⁺19] Hou Jiang, Ning Lu, Jun Qin, Wenjun Tang, and Ling Yao. A deep learning algorithm to estimate hourly global solar radiation from geostationary satellite data. *Renewable and Sustainable Energy Reviews*, 114:109327, 10 2019.
- [JLS11] S. Janjai, J. Laksanaboonsong, and T. Seesaard. Potential application of concentrating solar power systems for the generation of electricity in Thailand. *Applied Energy*, 88:4960–4967, 12 2011.
- [JMPL13] S. Janjai, I. Masiri, S. Pattarapanitchai, and J. Laksanaboonsong. Mapping global solar radiation from long-term satellite data in the tropics using an improved model. *International Journal of Photoenergy*, 2013:1–11, 2013.
- [KBSH18] Yashwant Kashyap, Ankit Bansal, Anil Kumar Sao, and Annette Hammer. Model for estimation of global horizontal irradiance in the presence of dust, fog, and clouds. *IEEE Transactions on Geoscience and Remote Sensing*, 56:7030–7037, 12 2018.
- [KMF⁺17] Guolin Ke, Qi Meng, Thomas Finley, Taifeng Wang, Wei Chen, Weidong Ma, Qiwei Ye, and Tie-Yan Liu. LightGBM: A highly efficient gradient boosting decision tree. In *Advances in Neural Information Processing Systems*, 2017.

- [LZC⁺23] Jingxuan Liu, Haixiang Zang, Lilin Cheng, Tao Ding, Zhinong Wei, and Guoqiang Sun. A transformer-based multimodal-learning framework using sky images for ultra-short-term solar irradiance forecasting. *Applied Energy*, 342:121160, 7 2023.
- [Mas22] Itsara Masiri. Development and improvement of potential solar energy map for thailand from satellite imageries (in thai). Technical report, Silpakorn University, 2022.
- [MC00] Kobrick Michael and Robert Crippen. SRTMGL1: NASA Shuttle Radar Topography Mission Global 1 arc second, 2000. Accessed: 2024-7-31.
- [NIK21] Andreas H. Nielsen, Alexandros Iosifidis, and Henrik Karstoft. IrradianceNet: Spatiotemporal deep learning model for satellite-derived solar irradiance short-term forecasting. *Solar Energy*, 228:659–669, 11 2021.
- [OB16] Manasseh Obi and Robert Bass. Trends and challenges of grid-connected photovoltaic systems – a review. *Renewable and Sustainable Energy Reviews*, 58:1082–1094, 5 2016.
- [PAL21] Quentin Paletta, Guillaume Arbod, and Joan Lasenby. Benchmarking of deep learning irradiance forecasting models from sky images – an in-depth analysis. *Solar Energy*, 224:855–867, 8 2021.
- [PAL23] Quentin Paletta, Guillaume Arbod, and Joan Lasenby. Omnivision forecasting: Combining satellite and sky images for improved deterministic and probabilistic intra-hour solar energy predictions. *Applied Energy*, 336:120818, 4 2023.
- [PFPS⁺20] Jesus Polo, Carlos Fernández-Peruchena, Vasileios Salamalikis, Luis Mazorra-Aguiar, Mathieu Turpin, Luis Martín-Pomares, Andreas Kazantzidis, Philippe Blanc, and Jan Remund. Benchmarking on improvement and site-adaptation techniques for modeled solar radiation datasets. *Solar Energy*, 201:469–479, 5 2020.
- [PH13] Richard Perez and Tom E. Hoff. *Solar Energy Forecasting and Resource Assessment*, chapter SolarAnywhere Forecasting, pages 233–265. Elsevier, 2013.
- [PHAL22] Quentin Paletta, Anthony Hu, Guillaume Arbod, and Joan Lasenby. Eclipse: Envisioning cloud induced perturbations in solar energy. *Applied Energy*, 326:119924, 2022.
- [PIM⁺02] Richard Perez, Pierre Ineichen, Kathy Moore, Marek Kmiecik, Cyril Chain, Ray George, and Frank Vignola. A new operational model for satellite-derived irradiances: description and validation. *Solar Energy*, 73:307–317, 11 2002.
- [PPGB13] Marius Paulescu, Eugenia Paulescu, Paul Gravila, and Viorel Badescu. *Weather Modeling and Forecasting of PV Systems Operation*. Springer London, 2013.
- [PSH⁺15] Richard Perez, James Schlemmer, Karl Hemker, Sergey Kivalov, Adam Kankiewicz, and Christian Gueymard. Satellite-to-irradiance modeling - a new version of the SUNY model. In *2015 IEEE 42nd Photovoltaic Specialist Conference (PVSC)*, pages 1–7. IEEE, 6 2015.
- [PSK⁺18] Richard Perez, James Schlemmer, Sergey Kivalov, John Dise, Patrick Keelin, Mark Grammatico, Thomas Hoff, and Aidan Tuohy. A new version of the SUNY solar forecast model: A scalable approach to site-specific model training, 2018.
- [PWRA⁺16] J. Polo, S. Wilbert, J.A. Ruiz-Arias, R. Meyer, C. Gueymard, M. Sári, L. Martín, T. Mieslinger, P. Blanc, I. Grant, J. Boland, P. Ineichen, J. Remund, R. Escobar, A. Troccoli, M. Sengupta, K.P. Nielsen, D. Renne, N. Geuder, and T. Cebecauer. Preliminary survey on site-adaptation techniques for satellite-derived and reanalysis solar radiation datasets. *Solar Energy*, 132:25–37, 7 2016.
- [QHM⁺19] Yi Qin, Jing Huang, Tim R. McVicar, Sam West, Maryam Khan, and Andrew D.L. Steven. Retrieving surface solar irradiance from Himawari-8: a physics based approach and its validation. In *2019 IEEE 46th Photovoltaic Specialists Conference (PVSC)*, pages 3164–3167. IEEE, 6 2019.
- [QHM⁺21] Yi Qin, Jing Huang, Tim R. McVicar, Sam West, Maryam Khan, and Andrew D.L. Steven. Estimating surface solar irradiance from geostationary Himawari-8 over Australia: A physics-based method with calibration. *Solar Energy*, 220:119–129, 5 2021.
- [QOB⁺17] Zhipeng Qu, Armel Oumbe, Philippe Blanc, Bella Espinar, Gerhard Gesell, Benoît Gschwind, Lars Klüser, Mireille Lefèvre, Laurent Saboret, Marion Schroedter-Homscheidt, and Lucien Wald. Fast radiative transfer parameterisation for assessing the surface solar irradiance: The Heliosat-4 method. *Meteorologische Zeitschrift*, 26:33–57, 2 2017.

- [QWL⁺18] Wenmin Qin, Lunche Wang, Aiwen Lin, Ming Zhang, Xiangao Xia, Bo Hu, and Zigeng Niu. Comparison of deterministic and data-driven models for solar radiation estimation in China. *Renewable and Sustainable Energy Reviews*, 81:579–594, 1 2018.
- [RAN12] Meita Rumbayan, Asifujang Abudureyimu, and Ken Nagasaka. Mapping of solar energy potential in Indonesia using artificial neural network and geographical information system. *Renewable and Sustainable Energy Reviews*, 16:1437–1449, 4 2012.
- [RLW04] C Rigollier, M Lefèvre, and L Wald. The method Heliosat-2 for deriving shortwave solar radiation from satellite images. *Solar Energy*, 77:159–169, 2004.
- [SBG⁺21] Xixi Sun, Jamie M. Bright, Christian A. Gueymard, Xinyu Bai, Brendan Acord, and Peng Wang. World-wide performance assessment of 95 direct and diffuse clear-sky irradiance models using principal component analysis. *Renewable and Sustainable Energy Reviews*, 135:110087, 1 2021.
- [SC10] Marcel Suri and Tomas Cebecauer. SolarGIS: New web-based service offering solar radiation data and PV simulation tools for Europe, North Africa and Middle East. In *Proceedings of the International Conference on Solar Heating*, pages 1–7, 2010.
- [SL18] Shikhar Srivastava and Stefan Lessmann. A comparative study of lstm neural networks in forecasting day-ahead global horizontal irradiance with satellite data. *Solar Energy*, 162:232–247, 3 2018.
- [SS16] Kais Siala and Jürgen Stich. Estimation of the PV potential in ASEAN with a high spatial and temporal resolution. *Renewable Energy*, 88:445–456, 4 2016.
- [Sta14] Brandon Stafford. Pysolar documentation, 2014.
- [STAK22] Vasileios Salamalikis, Panayiotis Tzoumanikas, Athanassios A. Argiriou, and Andreas Kazantzidis. Site adaptation of global horizontal irradiance from the Copernicus atmospheric monitoring service for radiation using supervised machine learning techniques. *Renewable Energy*, 195:92–106, 8 2022.
- [SWH⁺24] Suwichaya Suwanwimolkul, Wijarn Wangdee, Naebboon Hoonchareon, Nuttamon Thungka, Natanon Tongamrak, and Jitkomut Songsiri. Thailand solar irradiance map: Analysis of tree-based models. In *The 18th International Conference on Probabilistic Methods Applied to Power System (PMAP)*, pages 1–6. IEEE, 2024.
- [VPN⁺23] Enric Valor, Jesus Puchades, Raquel Niclos, Joan Miquel Galve Romero, Oriol Lacave, and Patricia Puig. Determination and evaluation of surface solar irradiance with the MAGIC-Heliosat method adapted to MTSAT-2/Imager and Himawari-8/AHI sensors. *IEEE Transactions on Geoscience and Remote Sensing*, 61:1–19, 2023.
- [VSDL⁺23] Hadrien Verbois, Yves-Marie Saint-Drenan, Quentin Libois, Yann Michel, Marie Cassas, Laurent Dubus, and Philippe Blanc. Improvement of satellite-derived surface solar irradiance estimations using spatio-temporal extrapolation with statistical learning. *Solar Energy*, 258:175–193, 7 2023.
- [VSP⁺17] Ashish Vaswani, Noam Shazeer, Niki Parmar, Jakob Uszkoreit, Llion Jones, Aidan N Gomez, Łukasz Kaiser, and Illia Polosukhin. Attention is all you need. In I. Guyon, U. Von Luxburg, S. Bengio, H. Wallach, R. Fergus, S. Vishwanathan, and R. Garnett, editors, *Advances in Neural Information Processing Systems*, volume 30. Curran Associates, Inc., 2017.
- [YB20] Dazhi Yang and Jamie M. Bright. Worldwide validation of 8 satellite-derived and reanalysis solar radiation products: A preliminary evaluation and overall metrics for hourly data over 27 years. *Solar Energy*, 210:3–19, 11 2020.
- [YCZ19] Yunjun Yu, Junfei Cao, and Jianyong Zhu. An lstm short-term solar irradiance forecasting under complicated weather conditions. *IEEE Access*, 7:145651–145666, 2019.
- [YDA⁺20] Jong-Min Yeom, Ravinesh C Deo, Jan F Adamowski, Seonyoung Park, and Chang-Suk Lee. Spatial mapping of short-term solar radiation prediction incorporating geostationary satellite images coupled with deep convolutional lstm networks for south korea. *Environmental Research Letters*, 15:094025, 9 2020.
- [ZWSW23] Liwenbo Zhang, Robin Wilson, Mark Sumner, and Yupeng Wu. Advanced multimodal fusion method for very short-term solar irradiance forecasting using sky images and meteorological data: A gate and transformer mechanism approach. *Renewable Energy*, 216:118952, 11 2023.
- [ZZP⁺20] Haoyi Zhou, Shanghang Zhang, Jieqi Peng, Shuai Zhang, Jianxin Li, Hui Xiong, and Wan Zhang. Informer: Beyond efficient transformer for long sequence time-series forecasting. In *AAAI Conference on Artificial Intelligence*, 2020.

Appendix: Supplementary results

Table 6 lists available services that provide satellite-derived solar irradiance. Table 7 shows the detailed estimation performance of the Informer model for each ground station. Figure 14 gives a comparative estimated solar energy map from Ministry of Energy that was discussed in Section 4.4.

Table 6: Satellite-derived solar irradiance services.

Service	Method	Web page
Global		
SolarAnywhere	SUNY model	https://www.solaranywhere.com/
NSRDB	Hybrid SUNY/METSTAT models	https://nsrdb.nrel.gov/
SolarGIS	SolarGIS satellite-to-irradiance model	https://solargis.com/
SolCast	SolCast cloud model	https://solcast.com/
GEWEX-SRB	Radiative transfer algorithm	https://science.larc.nasa.gov/gewex-srb/
Meteonorm 8	Stochastic generation of global radiation	https://meteonorm.com/
Vaisala	Vaisala algorithm (REST2/Krasen models)	https://www.vaisala.com/en
CM SAF (SARAH 3)	MAGICSOL	https://wui.cmsaf.eu/
Europe, Africa, and Parts of Asia and South America		
Soda-Pro	HelioClim-3 (Heliosat-2+McClear)	https://www.soda-pro.com/
Europe, Africa, and Parts of Asia, South America and Australia		
PVGIS	SARAH and NSRDB	https://pvgis.com/
CAMS Radiation service	McClear, McCloud models and Heliosat-4	https://atmosphere.copernicus.eu/
SOLEMI	Heliosat method	https://www.wdc.dlr.de/data-products/solar-radiation/solemi-data-base
Australia		
Australian Bureau of Meteorology	Physical model	http://www.bom.gov.au/climate/

Table 7: GHI estimation performance metrics of the Informer model split by ground stations. MAE, RMSE, MBE, \bar{I} are in W/m^2 and NMAE, NRMSE, NMBE are in %.

ID	Site name	MAE	RMSE	MBE	NMAE	NRMSE	NMBE	\bar{I}
Central								
1	Pathum Thani 1	71.71	109.81	-0.21	14.96	22.91	-0.04	479.32
2	Nakhon Pathom 1	115.36	174.97	-7.18	23.35	35.42	-1.45	494.03
3	Samut Prakan 1	93.56	149.26	15.90	19.47	31.07	3.31	480.47
4	Samut Prakan 2	73.55	115.33	-0.48	14.33	22.48	-0.09	513.12
5	Chachoengsao	80.48	120.07	7.84	15.95	23.80	1.55	504.49
6	Nonthaburi 1	107.18	168.64	3.77	21.93	34.51	0.77	488.70
7	Nakhon Sawan	79.97	120.04	-6.54	15.82	23.74	-1.29	505.65
8	Phra Nakhon Si Ayutthaya	77.72	123.52	-2.78	15.11	24.01	-0.54	514.37
10	Nonthaburi 2	79.60	123.01	3.65	15.76	24.36	0.72	504.91
11	Samut Prakan 3	76.21	114.40	6.72	14.94	22.42	1.32	510.20
33	Pathum Thani 2	80.26	122.39	12.81	16.10	24.55	2.57	498.46
35	Nakhon Pathom 2	73.42	115.35	-0.49	14.40	22.62	-0.10	510.01
36	Pathum Thani 3	73.03	112.39	-0.02	15.14	23.30	-0.00	482.43
42	Pathum Thani 4	79.13	125.13	7.37	15.22	24.06	1.42	520.07
46	Samut Prakan 4	67.04	103.97	-6.36	13.03	20.21	-1.24	514.39
47	Bangkok 1	82.89	122.37	16.66	18.38	27.13	3.69	451.05
48	Bangkok 2	73.99	111.52	16.96	15.81	23.82	3.62	468.12
56	Samut Sakhon	61.68	103.12	7.82	11.65	19.48	1.48	529.49
North								
9	Phrae	73.68	117.37	-9.74	14.75	23.50	-1.95	499.46
15	Lampang	78.89	124.89	25.24	16.01	25.34	5.12	492.87
19	Sukhothai	68.24	111.59	-1.55	12.99	21.24	-0.30	525.40
20	Lamphun	70.01	111.42	5.81	13.87	22.08	1.15	504.70
27	Chiang Mai 1	76.71	123.49	-0.45	13.90	22.38	-0.08	551.72
28	Chiang Mai 2	77.01	129.11	-1.80	15.07	25.26	-0.35	511.03
38	Phetchabun 1	77.26	125.28	-1.37	15.02	24.35	-0.27	514.42
43	Phetchabun 2	68.89	111.56	7.04	13.38	21.66	1.37	515.07
NorthEast								
12	Yasothon	70.24	111.73	5.66	13.41	21.33	1.08	523.92
13	Ubon Ratchathani	112.93	154.23	1.33	23.80	32.50	0.28	474.52
17	Buriram	80.50	122.44	6.77	16.20	24.64	1.36	496.92
18	Kalasin	122.08	186.83	16.75	24.38	37.30	3.34	500.85
21	Udon Thani	98.28	150.02	17.39	19.90	30.38	3.52	493.84
22	Khon Kaen	71.75	116.13	7.55	13.43	21.74	1.41	534.24
25	Chaiyaphum	62.80	100.47	-7.24	11.83	18.92	-1.36	531.02
26	Nakhon Ratchasima 1	72.83	119.11	5.90	14.16	23.16	1.15	514.34
30	Nakhon Ratchasima 2	79.85	128.24	15.90	15.59	25.03	3.10	512.33
31	Sakon Nakhon 1	67.72	112.70	-0.10	13.67	22.75	-0.02	495.27
39	Sakon Nakhon 2	88.73	137.80	18.89	17.21	26.73	3.66	515.52
41	Roi Et	74.98	121.24	14.23	14.37	23.24	2.73	521.80
East								
23	Chonburi 1	71.68	117.43	-11.20	14.24	23.33	-2.22	503.30
24	Chanthaburi	86.62	136.04	-8.11	18.83	29.57	-1.76	459.98
40	Chonburi 2	74.47	120.37	0.11	15.55	25.14	0.02	478.84
44	Sa Kaeo	79.83	121.06	-7.05	15.74	23.87	-1.39	507.25
49	Chonburi 3	71.88	110.06	16.03	15.11	23.14	3.37	475.70
50	Chonburi 4	71.60	117.32	2.53	14.41	23.62	0.51	496.79
51	Chonburi 5	66.96	106.10	-0.84	13.56	21.48	-0.17	493.91
52	Chonburi 6	76.58	113.42	14.25	17.14	25.39	3.19	446.67
53	Chonburi 7	81.64	121.07	-1.96	16.82	24.94	-0.40	485.35
55	Chonburi 8	70.57	106.89	8.06	14.52	21.99	1.66	486.15
West								
16	Ratchaburi	77.59	122.36	4.73	15.31	24.15	0.93	506.72
37	Phetchaburi	65.51	105.03	-2.07	12.46	19.98	-0.39	525.78
South								
14	Surat Thani	96.81	141.02	10.14	20.80	30.29	2.18	465.56
29	Krabi	90.63	139.25	13.97	18.26	28.05	2.81	496.39
34	Nakhon Si Thammarat	90.98	133.65	-0.32	18.91	27.78	-0.07	481.08

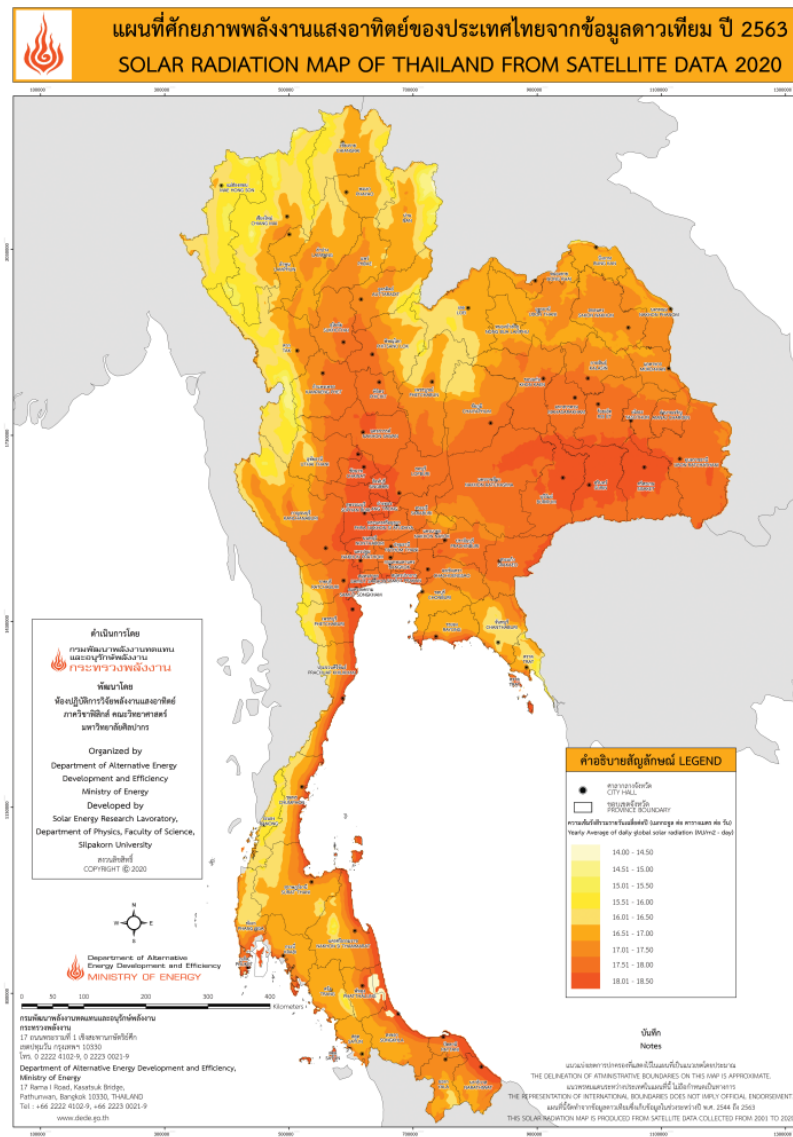


Figure 14: Solar radiation map of 2023, provided by Ministry of Energy (Source: https://gis.dede.go.th/upload/20230302_135735.pdf). The map shows yearly average of daily global radiation ($\text{MJ/m}^2 \cdot \text{day}$).

We can convert the yearly average of daily global radiation ($\text{MJ/m}^2 \cdot \text{day}$) in Figure 14 by multiplying $0.2778 \cdot 365$ to be the unit of kWh/m^2 as to compared with Figure 13a (total yearly energy). For example, the hottest and coldest spots in Figure 14 are 18.50 and $14.00 \text{ MJ/m}^2 \cdot \text{day}$, respectively, and they correspond to the total yearly energy of 1875.84 and 1419.56 kWh/m^2 (which can be compared to values in Figure 13a). As to compare with Figure 14, our estimated map in Figure 13a has a similar trend of spatially relative energy while an actual value of yearly energy estimate at a specific location (except in northeastern) appears to be higher.